The response of buoyant plumes to transient discharges investigated using an adaptive solver.

J. O'Callaghan, G. Rickard, S. Popinet, and C. Stevens.

National Institute of Water and Atmosphere, Wellington, New Zealand.

J. O'Callaghan, National Institute of Water and Atmosphere, Private Bag 14-901, Wellington, New Zealand.(j.ocallaghan@niwa.co.nz)

Abstract. The behavior of buoyant plumes driven by variable momentum inputs were examined using an adaptive Navier-Stokes solver (Gerris). Boundary conditions were representative of an idealized stratified, coastal environment. Salinity ranged from 5 to 30 in the top 5 m of the water column to replicate the strong vertical gradients experienced in fjord environments. Two-dimensional simulations examined the response of the buoyant plume driven by zero, steady and variable momentum fluxes. The behavior was quantified in terms of the characteristic features of a buoyant plume, the thickness of the nose (or head of gravity current) and the trailing tail. Both the nose and tail of the plume were substantially thicker for the variable momentum run, whereas elongation and thinning of the plume was evident for the steady and zero momentum inputs. Furthermore, an order of magnitude difference in available potential energy was found for the variable momentum run. Validation of the Boussinesq approximation initially utilized the classic lock-exchange experiment with excellent agreement to previous numerical and theoretical experiments. Frontal speeds of the gravity current converged towards the theoretical value of Benjamin [1968]. The adaptive mesh permitted lock-exchange simulations at Re of $\sim 2 \times 10^6$ and are some of the highest Re runs to date. Moreover, improved computational efficiency was achieved using the adaptive solver with simulations completed in 20 % of the time they took on a static, high-resolution grid.

1. Introduction

Buoyant river plumes entering the coastal ocean are a mixture of suspended materials, buoyancy and kinetic energy that occupy a thin lens typically only several meters deep at the surface of the ocean. The evolution of steady plumes has, so far, received the greatest attention, yet discharges of river water are inherently event-driven by storms and anything but steady. Moreover, these freshwater discharges are modulated by the regular tidal oscillations [Nash and Moum, 2005]. Although plume separation, resultant density structure and advection of the far-field plume are regulated by river discharges [Garvine, 1999; Yankovsky et al., 2001], our understanding of how the incoming buoyancy and energy are redistributed in the near-field environment is poor. The transient nature of freshwater discharges make timely measurements an additional challenge to those imposed in the highly sheared and stratified near-field region. Accurate representation of the wide ranging time and space scales of this problem remain an unresolved challenge for most contemporary numerical models. Here we seek to address this limited understanding of energy conversion by examining what aspects of near-field mechanics regulate the structure of the buoyant plume with an adaptive numerical model.

At frontal boundaries, the manner with which the buoyant discharge mixes in the near-field underpins the plume structure that propagates into the far-field, and ultimately coastal circulation patterns. Initial density gradients and thickness of the near-field gravity current cause variations in salinity concentrations and influence the resultant size of the plume [Nash et al., 2009; Horner-Devine, 2009]. There are, however, only a sparse number of observations in this crucial region. Luketina and Imberger [1989] made the first fine-

scale observations in an active turbulent mixing zone and although there were only a handful of measurements from a moored instrument, they were able to identify a strongly sheared mixing layer several meters below the surface layer in the roller region. Turbulence generated in the active mixing zone via Kelvin-Helmholtz instabilities becomes advected downstream by super-critical flow [Luketina and Imberger, 1987; MacDonald and Geyer, 2004]. Observations from the Connecticut River were used to quantify dissipation rates, ϵ, across the plume front with rates that decreased from 10^{-3} to 10^{-6} Wkg^{-1} within the first 100 m [O'Donnell et al., 2008]. The only other data available came from the larger Columbia River plume. Unsurprisingly, the Columbia River plume had a larger zone of active mixing and higher rates of ϵ [Orton and Jay, 2005].

The near-field of buoyant jets (plumes with momentum) is characterized by active mixing that entrains ambient water into the core of the plume via shear instabilities. Several metrics exist for determining the length scale of the mixing region, in the absence of greater quantities of turbulence data. Engineering texts estimate the transition from intense vertical mixing to lateral spreading of the plume within $\sim L_M$ based on external parameters of flow discharge ($L_M = M^{3/4}/B^{1/2}$, M = momentum flux and B = buoyancy flux Fischer et al. [1979]). From laboratory experiments, shear-induced mixing of turbulent energy was found to decay to a zero vertical flux within five buoyancy periods from the generation location [Itsweire et al., 1993]. Using observations from the plumes described above, this relationship of $L_I \sim 5U/N$ (U = mean velocity and N = buoyancy frequency) was adhered to by both the small and large river plumes [O'Donnell et al., 2008; Orton and Jay, 2005] indicating the underpinning mechanics for plumes of different scales is retained despite differences in turbulent dissipation rates. An alternate measure of the

spatial influence of active mixing, L_G, was proposed in an early model by Garvine [1987], whereby the magnitude of vertical mixing decayed exponentially with distance from the plume front ($\epsilon(x) = \epsilon_o exp(-x/L_G)$). The large number of estimates of turbulent dissipation rates obtained from towed instrumentation in the Connecticut plume facilitated the first in situ validation of L_G and, encouragingly, was the same order of magnitude as L_I for the system [O'Donnell et al., 2008].

Beyond the active mixing zone, the buoyant discharge spreads laterally, forming along-coast circular bulges. In this intermediate-to-far-field zone, competition between wind, tide and Coriolis forcing influences the spatial extent of a bulge [Fong and Geyer, 2002], bulge recirculation [Horner-Devine, 2009] and magnitude of coastal currents [Hickey et al., 2005]. It is these, relatively, well-measured far-field processes that modelling efforts have been aligned to. Typically, the shelf and coastal zone have been idealized as rectangular with a narrow slit along one side for the river outlet (see Garvine [1999]; Fong and Geyer [2002]). Using an estuarine version of the Princeton Ocean Model (POM) plume evolution with and without wind-stress, varying Coriolis and with steady discharges were examined for the Delaware [Whitney and Garvine, 2006], Po [Kourafalou et al., 1996] and Connecticut coastal systems [O'Donnell, 1990]. Model outputs generally agreed with available field or satellite observations. However, in these studies small-scale mixing at frontal zones was either not included or inadequately resolved by the model due to limited understanding of mixing at the estuary-coast boundary. Most recently, buoyancy fluxes across the Columbia River plume front were determined using the Regional Ocean Modelling System (ROMS, MacCready et al. [2008]). Although the model ϵ spanned 3 orders of magnitude, as per field observations, overestimates by the model at higher densities were attributed to sam-

pling inconsistencies of inhomogeneous turbulence in the near-field. The need for coupled plume-estuary coastal models for improved representation of the complex physics, rather than the more simple outlet approach of earlier studies was also highlighted [MacCready et al., 2008].

Interactions between the small-scale mixing and larger-scale processes lie at the heart of how material is transported and redistributed. The use of non-hydrostatic models to simulate the full spectrum of scales is an appealing way forward. For example, Stashchuk and Vlasenko [2009] used the Massachusetts Institute of Technology general circulation model (MITgcm, Marshall et al. [1997]) to capture the short non-linear internal waves (IWs) generated by the Columbia River plume [Nash and Moum, 2005]. An alternative pathway – and the one adopted herein – is the use of adaptive models. These models are capable of resolving processes at a range of scales with greater computational efficiency than a static non-hydrostatic code. Gerris is an incompressible Navier–Stokes solver with spatial resolution varying in both space and time [Popinet, 2003, 2009] and has been applied to geophysical problems [Popinet et al, 2004; Popinet and Rickard, 2007]. Gerris uses an octree grid structure in contrast to other models such as the Imperial college ocean model (ICOM, Pain et al. [2005]) or Stanford unstructured non-hydrostatic numerical terrain following Navier–Stokes simulator (SUNTANS, Fringer et al. [2006]) which adopt an unstructured grid that allows for sufficient detail to be retained along complex coastlines [Wang et al., 2008]. Staircase resolution of bathymetry in the vertical and the computational expense for mass conservation make the latter model not yet adaptive in time (i.e. the spatial resolution is fixed during the course of the simulation). The finite-volume, tree-based, spatial discretization of Gerris provides similar flexibility

to a fully unstructured grid while preserving the simplicity and conceptual framework of Cartesian grids [Popinet, 2003, 2006, 2009]. Dynamic refinement of either the quad (two-dimensional, 2D) or octree (three-dimensional, 3D) at each time step was found to be only a small fraction of the total computational cost. The adaptive mesh in Gerris reduces computing times by several orders of magnitude for barotropic simulations at coastal scales [Popinet and Rickard, 2007] and Navier–Stokes simulations of internal wave breaking at laboratory scales [Rickard et al., 2009].

In this article, our main objective was to examine how varying inputs of momentum and buoyancy influenced the near-field plume structure using an adaptive modelling tool. Plume thickness and density of the buoyant gravity current are ultimately modified by a medley of processes in the far-field environment. This extends the barotropic work of Popinet and Rickard [2007] to develop the capability of the adaptive model to simulate baroclinic processes at the laboratory and coastal scale. Validation of simulations that utilize the Boussinesq approximation is a key element of plume mechanics. To this end, we consider the behavior of the classic lock-exchange to be the most relevant problem for validation since it is characterized by large-scale gravity current propagation along with small-scale shear instabilities at the density interface. The remainder of this paper is constructed as follows. Section 2 presents the equations used by the Gerris solver. Section 3 outlines the details of the classic lock-exchange test case for validation of Boussinesq flows in Gerris. Outputs of the buoyant plume simulations are shown in Section 4, where the role of buoyancy only, steady and variable momentum inputs on near-field structure are examined. Implications for transient coastal plumes will be discussed in Section 5, with a summary given in section 6.

2. The Gerris Flow Solver

Gerris is an adaptive, finite-volume, incompressible, Navier–Stokes fluid solver [Popinet, 2003, 2009], which has recently been shown to be also an efficient adaptive barotropic ocean model [Popinet and Rickard, 2007]. In this paper, the governing equations in non-dimensional form solved by Gerris are:

$$\frac{\partial u}{\partial x} + \frac{\partial v}{\partial y} = 0 \tag{1}$$

$$\frac{\partial u}{\partial t} + u\frac{\partial u}{\partial x} + v\frac{\partial u}{\partial y} = -\frac{\partial p}{\partial x} + \frac{1}{\mathrm{Re}}\left(\frac{\partial^2 u}{\partial x^2} + \frac{\partial^2 u}{\partial y^2}\right) \tag{2}$$

$$\frac{\partial v}{\partial t} + u\frac{\partial v}{\partial x} + v\frac{\partial v}{\partial y} = -\frac{\partial p}{\partial y} + \frac{1}{\mathrm{Re}}\left(\frac{\partial^2 v}{\partial x^2} + \frac{\partial^2 v}{\partial y^2}\right) + \frac{1}{\mathrm{Fr}^2}T \tag{3}$$

$$\frac{\partial T}{\partial t} + \frac{\partial (uT)}{\partial x} + \frac{\partial (vT)}{\partial y} = \frac{1}{\mathrm{RePr}}\left(\frac{\partial^2 T}{\partial x^2} + \frac{\partial^2 T}{\partial y^2}\right). \tag{4}$$

Here u and v denote the velocity vectors in the horizontal and vertical directions, respectively and p is pressure. Re is the Reynolds number $\mathrm{Re} = \mathrm{UL}/\nu$ where U is a characteristic flow speed, L is the length of the domain, ν is the kinematic viscosity. The Froude number is given by $\mathrm{Fr} = \mathrm{u}/\sqrt{\mathrm{g'L}}$ where g′ is reduced gravity $\mathrm{g'} = \mathrm{g}(\rho - \rho_\mathrm{o})/\rho_\mathrm{o}$. With g the acceleration due to gravity, ρ is density, and ρ_o the reference density. T is a tracer (as temperature and/ salinity) and is specified by one or more functions, or the equation of state. It was non-dimensionalized by a scalar (either temperature, salinity, or both) and together with $1/\mathrm{Fr}^2$, the last term in equation 3 represents the densimetric Fr number

widely used in the context of Boussinesq flows. Finally, the Prandtl number $\mathrm{Pr} = \nu/\kappa$ is the ratio of kinematic viscosity and molecular diffusivity of temperature κ.

By default, a Gerris domain is a square (2D) or a cube (3D) of edge length unity. The spatial discretization is either a quadtree or octree structure with individual cells being square Cartesian finite-volume elements. The cells are arranged hierarchically with each cell able to be the parent of up to four children in 2D (eight in 3D). Quadtree (octree) cell structure is isotropic and can refine and coarsen in all directions simultaneously to user-defined criteria. In the following we have used two criteria. The vorticity criterion:

$$\frac{|\nabla \times \mathrm{u}|\Delta}{\max(|\mathrm{u}|)} < \epsilon \tag{5}$$

with Δ the mesh size and ϵ a user-defined threshold, will ensure that a finer resolution is used in areas of high vorticity. The typical threshold is set to 10^{-2} for vorticity and 10^{-1} for tracers.

The gradient criterion:

$$|\nabla c|\Delta < \epsilon \tag{6}$$

with c the user-defined tracer/s and ensures that strong tracer gradients will be tracked with higher resolution.

In the following results, we consider a laboratory ($\mathrm{L} \sim 1$ m) and field-scale ($\mathrm{L} \sim 100$ m) problem. The associated Reynolds numbers vary in proportion to these length scales (1 to 100). While we demonstrate that reasonably fast direct numerical simulations (DNS) can be performed for the laboratory-scale problem, this is not the case for the field-scale problem. If DNS cannot be used, by definition some turbulence closure scheme needs

to be used to model the unresolved subgrid-scale (SGS) processes. Turbulent closure schemes are the subject of many papers and on-going research (see Burchard [2002] for a good review), yet much conjecture exists about which approach to implement. Popinet et al [2004] investigated using the numerical dissipation of Gerris as the simplest closure scheme (an approach known as MILES or monotonically integrated large eddy simulation, Grinstein and Fureby [2002]). Good agreement was found between numerical and field turbulence spectra. This is the approach we have used for the field-scale problem in the present paper.

3. Laboratory scale: The lock-exchange problem

3.1. Model validation and set-up

Validation of non-hydrostatic models has typically used the lock-exchange problem [Bourgault and Kelley, 2004; Berntsen et al., 2006]. This classical laboratory experiment will also be used here to validate both small scales (non-hydrostatic) flows and the Boussinesq approximation in Gerris. In the laboratory, a rectangular tank/channel is partitioned by a gate with fluid of two different densities either side of the gate. When this gate (or lock) is removed, intrusions of these fluids in opposite directions manifest themselves as gravity currents along the horizontal boundaries of the tank [Simpson, 1997]. Shear instabilities across the density interface, coupled with gravity current propagation provides a robust test for the model since processes span the small- and large-scale. In addition, the computational efficiency of direct numerical simulations (DNS) using the adaptive model can be compared to previously published DNS results obtained using static grids for the widely used lock-exchange problem. Frontal speeds and structure of the gravity current

were first characterized using laboratory experiments [Benjamin , 1968] that remain valid benchmarks for numerical simulations [i.e. Härtel et al., 2000].

To allow the set-up of gravity currents along a channel the domain must be sufficiently long [Härtel et al., 2000]. Here, the domain is a series of 12 boxes positioned side-by-side in the x-direction. The dimensional length/height of each box was set to 0.2 m and results in a dimensional domain of 0.2 x 2.4 m, akin to laboratory experiments conducted by Maxworthy et al. [2002]. The lock-exchange problem was initialized with a flow field at rest everywhere, i.e. u and v = 0. The initial tracer field consisted of a volume of heavy and light density in the left and right half of the rectangular channel, respectively (Fig. 2) and was given by:

$$T(x) = \frac{1}{2} - \frac{1}{2}\mathrm{erf}\left(\mathrm{x}\sqrt[4]{GrPr^2}\right) \tag{7}$$

where Gr is the Grashof number, the ratio of buoyancy and viscous forces (based on an estimate of buoyancy velocity from the initial density gradient in the domain) and $\mathrm{Gr} = \left(\mathrm{u_b h}/\nu\right)^2$ [Härtel et al., 1997]. The buoyancy velocity is determined using $\mathrm{u_b} \sim \sqrt{\mathrm{g'h}}$. The Re number is an externally imposed number through $\sqrt{\mathrm{Gr}} \sim \mathrm{Re}$ in the momentum equation. Pr number of ~ 7 was used for all simulations based on ν of 1 $\times 10^{-6} \mathrm{m^2 s^{-1}}$ and κ of 1.4 $\times 10^{-6}$ $\mathrm{m^2 s^{-1}}$. Frontal Re were quantified from simulations by $\mathrm{Re_f} = \mathrm{u_f h_f}/\nu$, where $\mathrm{u_f}$ and $\mathrm{h_f}$ are the speed and height of the gravity current following Härtel et al. [1997]. Lock-exchange simulations spanned three orders of magnitude of Re (Gr), with the details for both non-dimensional numbers and viscosity in Table 1.

All simulations were 2D with slip or no-slip boundary conditions implemented at each Re number specified. The use of the no-slip boundary condition allowed us to compare

with LES [Ozgokmen et al., 2007], DNS [Härtel et al., 1997] and laboratory experiments of gravity currents [Simpson, 1979]. Slip boundary conditions were also implemented, as is commonly done when density gradients are relatively small [Härtel et al., 1997], to examine flows where less dense water disperses along the free surface of higher density water as is the case for buoyant river plumes.

Adaptive mesh refinement (AMR) was used for the majority of runs, with a quadtree that ranged from an initial level of 5 (i.e. $2^5 = 32$ grid points per unit length) up to a maximum level of 9 ($2^9 = 512$ grid points). For the scale length of L = 0.2 m, these quadtree levels corresponded to maximum and minimum cell sizes of $0.2/2^5 \sim 6.25$ mm and $0.2/2^9 \sim 0.4$ mm, respectively. This minimum cell size was chosen so that $\triangle x \sim (GrPr^2)^{-0.25}$ as outlined Härtel et al. [1997], who proposed that full spectrum of temperature dissipation could be resolved if this criteria was met. For the largest Re (~ 10500) used in this study $\triangle x \sim 2.4$ mm and larger than the minimum resolution of simulations with quadtree level of 9. A convergence test to the theoretical limit outlined by Benjamin [1968] for Re ~ 10500 was investigated to cross-validate this criteria. Several simulations were also completed without adaptivity and are equivalent to previous high-resolution static grid simulations. Uniform cells at the highest quadtree level of 9 were used at all time steps to evaluate the computational gain of dynamic spatial discretization.

3.2. Gravity current behavior induced by lock-exchange

The transition from laminar to turbulent flow in the lock-exchange occurs when Re is greater than ~ 600 [Simpson, 1997], with an observed change between approximately 350 to about 730 from numerical simulations [Berntsen et al., 2006]. Isocontours of density for the three simulations, with no-slip boundary conditions, followed this convention, with Re

~ 300 displaying laminar behavior. Kelvin-Helmholtz (KH) instabilities along the density interface do occur even at the lowest Re. Certainly by Re ~ 2600 flow was turbulent with KH billows present, along with a strong vortex immediately behind the nose of the front. Vortex shedding and rapid entrainment was apparent for the highest Re of 10500 (Fig. 2c). Snapshots of the gravity current at the two higher Re showed remarkably similar locations of the frontal region, or nose of the front, but the position for the lowest Re lagged slightly behind the turbulent gravity currents.

Simulations at the highest Re captured a greater range of length scales that were not present in Fig. 2a and b. Two-dimensional LES simulations conducted by Ooi et al. [2007] also found a similar behavior of small-scale eddies within large-scale billows. They suggested that these were an initial decay of the larger vortices in 2D. But since energy decay is a 3D process it is more likely that what we saw in Fig. 2c was increasingly finer scale KH instabilities within the larger KH billows for the highest Re run.

Turbulent runs differed from the laminar flow by the presence of several small vortices along the nose of the gravity current. For the highest Re (~ 10500) the smaller two-dimensional vortices disturb and modify the larger structure of the KH billows in a similar way to the Ooi et al. [2007] simulations at a slightly higher Re than was used in our study. It is worth noting that our simulations are some of the highest Re conducted for the lock-exchange problem, with comparisons only possible to Ooi et al. [2007]. Many of the same features were replicated for slip boundary conditions; the main difference without friction was that the nose of the gravity current was located right on the boundary. Hence, instabilities could not grow behind the foremost part of the nose. For brevity the slip results are not shown, but were included in the convergence test.

Time-dependent positions of the gravity current nose for each Re number (Fig. 2) allowed us to quantify the frontal speed, u_f, for comparison to other studies. Frontal speeds (Re_f in brackets) were 0.54 (300), 0.607 (2600) and 0.625 (10500) ms^{-1} for no-slip conditions. Slightly faster u_f were seen in the absence of friction at the boundaries. According to Härtel et al. [2000], based on the early experiments by Simpson [1979], u_f should be ~ 0.65 immediately behind the frontal zone. Although speeds were higher for slip conditions (~ 0.67) the relationship whereby gravity current speeds immediately behind the nose are ~ 1.1 times u_f was valid in the absence of friction.

At the boundaries friction forced the dynamics at and below the foremost position of the gravity current to differ from slip conditions (Fig. 2a and b show the slip and no-slip simulations, respectively). A close examination of the frontal region at Re = 10500 shows the presence (and absence) of a small intrusion of low density fluid below and behind the head of the gravity current. These instabilities – or stagnation points [Härtel et al., 2000] – are distinct from the frontal position. In subsequent snapshots (not shown), the small-scale features appear to be entrained into the propagating gravity current, slowing the frontal speed slightly. However, in Fig. 2a the presence of static instabilities at the boundary downstream from the stagnation point seem related to the instabilities near to the frontal region, concurring with [Härtel et al., 2000] who postulated that the available energy at the stagnation point can trigger buoyancy-driven instabilities along the boundaries. It is interesting to note that the magnitude of instabilities were greatest for the higher Re simulations. Due to the proximity of the boundary. these features are difficult to quantify (hence compare to) with current techniques used in laboratory experiments. An example of the adaptive mesh grid that corresponds to Fig. 2b is shown in Fig. 2b.

3.3. Assessment of the Gerris model

Before extending this adaptive model to field scales, it is instructive to evaluate how well the physics are represented when L $\sim$ 1 m. An assessment of the efficiency of the adaptive scheme is left for the discussion. At this length scale, the full spectrum of processes can be resolved by the model. Convergence of model solutions towards the classical, inviscid theoretical value of Benjamin [1968] is based on the relationship that viscous forces slow the propagation speed of the gravity current at higher Re number. This is a robust evaluation that the physics observed in laboratory experiments are captured by a model and has been widely used by other DNS and non-hydrostatic codes by comparing Re to Fr number for the lock-exchange problem (i.e. Härtel et al. [2000]; Berntsen et al. [2006]).

Thus, the convergence of Gerris outputs for both slip and no-slip boundary conditions to $1/\sqrt{2}$ were very encouraging (Fig. 2). Not only did the normalized Fr from the adaptive simulations tend to the theoretical value of Benjamin [1968], but values were also similar to the 2D DNS by Härtel et al. [1997] for the no-slip conditions. Slightly faster frontal speeds were evident when the boundaries were frictionless, akin to the slip conditions implemented in Härtel et al. [2000]. For comparison, values from the modified non-hydrostatic codes [Berntsen et al., 2006] were included in Fig. 2. Although these models also converged to the classical theoretical value, a closer inspection of the model output showed that only the large scale features of the gravity current were simulated. The small-scale overturns below the nose which characterize the stagnation point and clearly observed in Gerris (Fig. 2a) were not captured. This suggests that the smallest scales, or turbulence, are underrepresented in the modified non-hydrostatic codes which is indicated by the slightly faster frontal speeds.

Gerris showed an accurate representation of the gravity current induced by lock-exchange. Large-scale frontal speeds converged towards laboratory benchmarks. Coupled with the small-scale instabilities at the nose of the gravity current and static instabilities present along the boundaries at higher Re, the multiscale nature of the problem was realized by the model. This validation of buoyancy-driven flow gave us confidence in subsequent simulations of field-scale buoyant plumes.

4. Field scale: The buoyant plume

4.1. Physical context for simulations

A framework for investigating buoyant plume mechanics was motivated by observations (unpublished) in Doubtful Sound, Fiordland, New Zealand. The reasons for choosing this system were two-fold. First, fjords experience many of the physical processes of the coastal ocean, yet the narrow topography allows the problem to be reduced to two-dimensions. Second, this fjord is subjected to substantial, transient outflows from the local hydro-electric scheme which initiate a buoyant jet/plume [Gibbs et al., 2000] . The injection of large quantities of low-salinity water into the headwaters at variable rates between 350 to 500 m^3s^{-1} mimics pulsed, high flow rate discharges from major rivers in New Zealand and elsewhere [MacDonald and Geyer, 2004]. Salinity stratification of ambient water exhibits strong near-surface gradients with vertical differences in excess of ~ 30 over the top 5 to 7 m of the water column. These strong vertical salinity gradients, coupled with variable momentum inputs, provided the parameter space over which the mechanics of transient buoyant plumes were investigated at coastal scales, albeit in an idealized context.

4.2. Parameter space for the buoyant plume

The dimensional scale length of the Gerris domain was set to L = 50 m (an order of magnitude than the laboratory problem), with 8 Gerris boxes positioned side-by-side to form a rectangular domain of 50 x 400 m. Initial temperature and salinity gradients were based on stratification in Doubtful Sound [Gibbs et al., 2000] and were given by:

$$\mathrm{T(y)} = 15.0 - 3.0(1.0 + \tanh((\mathrm{y} - 0.49)/0.07)) \tag{8}$$

$$\mathrm{S(y)} = 35.0 - 22.0(1.0 + \tanh((\mathrm{y} - 0.49)/0.07)) \tag{9}$$

Salinity gradients ranged from 10.28 to 35.0 in the vertical with strongest $\partial S/\partial z$ over the top 5 m. The top and bottom temperatures were 11.68 and 15.0 ^{o}C, respectively. The equation of state was that described in McDougall et al. [2003]. Three runs constitute the key mechanics of gravity currents in a stratified fluid. The first simulation was initiated without momentum; buoyancy-driven flow was generated by a large density gradient between low density water at the left boundary and ambient stratification similar to experiments conducted by Maxworthy et al. [2002]. The other two runs used a Gaussian velocity profile that injected brackish (5), cold water (11 ^{o}C) into the domain, with one ramping up to a constant input velocity and the other had variable inflow velocities to replicate the transient nature of river discharges or hydroelectric discharges (see Fig. 2).

All simulations were 2D and a rigid-lid was imposed at the surface. Three pseudo-moorings were located in the simulations at 25, 75 and 200 m from the left-hand boundary (see vertical lines in Fig. 2a). The time series of u, v, salinity, temperature at five heights – 2.5, 5, 7.5, 15 and 35 m from the surface – were post-processed to better understand the competition between shear, stratification and mixing for the three runs. Rotation was

not included in these simulations as the primary focus was to understand the small-scale structure at the head of plume/frontal region that is independent of rotation in the near-field [Garvine, 1974]. For mass conservation, the right boundary was equivalent to the left boundary with the outflow of momentum concentrated in the top 5 m.

Although there are benefits gained by using AMR [Popinet and Rickard, 2007; Rickard et al., 2009], adaptivity is an additional parameter to understand in model outputs. Since knowledge pertaining to near-field plume mechanics is limited due to few observations and sparse output from other models, our simulations did not initially use adaptivity. Gains in computational efficiency can still be made by specifying non-uniform, static quadtree levels where required. Since stratification was strongest near the surface a quadtree level of 9 was specified for the top 12.5 m and a refinement level of 6 in the lower 37.5 m. The minimum and maximum cell size was 0.03 and 0.6 m, respectively. An adaptive run, for the steady momentum run, was completed to quantify the computational benefit of AMR.

4.3. Buoyancy only

In the absence of momentum, a buoyant plume (or gravity current) developed within 50 s of the simulation starting (Fig. 2a). Initial gradients in density were large and mechanics observed in the lock-exchange validation were replicated here as the unstable vertical and horizontal density worked towards equilibrium. By 200 s, the buoyant plume closely resembled, as expected, the lock-exchange gravity current with the characteristic nose and tail structure present. Rapid entrainment of the less dense water into the ambient fluid dominated dynamics early in the simulation. This resulted in advection of the newly formed plume away from the source with strong return flows along the base of the plume. The thickness of the nose was 3 to 4 m from the top of the domain. KH billows were

present along the top of the pycnocline with the most coherent billows nearest to the left (or input) boundary. Although velocities at the nose had increased by $\sim 5\%$ a short time later (t = 400 s), the nose of the plume had thinned substantially and the vertical depression (or plume thickness) of the pycnocline was within 0.5 m of the surface (Fig. 2c).

4.4. Steady and variable momentum

Inflows, for the steady and time-variable momentum, were concentrated in the top 5 m, with maximum flows when the peak of the Gaussian curve intersected the top of the domain. Below this depth, inputs of both buoyancy and momentum were zero. Time series of maximum momentum inputs (near to the top boundary) are shown in Fig. 2. For both steady and variable momentum, velocity was ramped to a maximum of 1 ms^{-1} within 5 s. This peak was maintained for the remainder of the simulation for steady momentum, but decreased to near zero between 100 and 150 s for the variable momentum. The second velocity peak spanned 150 to 200 s with a subsequent decrease to near zero again. Although a longer domain would have been preferred, the CPU time to complete 5000 time steps, or 300 s, was already high at $\sim$ 92 hours for a 50 x 400 m domain. Readjustment of the parameter space was considered, i.e. smaller Re numbers, however maintaining maximum near-field resolution was a priority. Therefore, to evaluate plume response to variable momentum, inputs had to lie within this constraint of less than 400 s for a input velocity of 1 ms^{-1}.

Initial stratification for both the steady and variable momentum runs is shown in Fig. 2a. Unsurprisingly, the addition of momentum increased the propagation speed of the gravity current (Fig. 2b). Greater vertical intrusions of the plume and faster propagation times were evident for these runs (compared to the buoyancy only run). The

plume thickness for all three runs showed a clear decrease in h_f for buoyancy only, some minor variations for steady momentum, and an increased thickness in gravity current head for the time-variable run (Fig. 2). Associated speeds of the gravity current were determined from the positional history of the plume nose (data not shown), with the addition of momentum responsible for a $\sim 30\%$ increase of its mean speed (from 0.675 to 0.97 ms^{-1}). Further increases in plume speed became evident for the variable momentum case with speeds up to 1.12 ms^{-1}.

Variations in small-scale instabilities were the key difference between the steady and variable momentum runs. By examining Fig. 2d and e, the thickness (same as h_f in Fig. 2b) of the low-salinity water was greater in the near-field plume environment for the variable momentum inputs. At 25 m from the source the thickness of low-salinity water occupied only 1.65 m for the steady case, but increased to 5.2 m for the variable momentum run. Greater compression of the isohalines occurred in the first $\sim$ 75 m of the domain, while further downstream an increased number of KH billows were present along the top isohaline. Of note were the relatively large, multiple oscillations along the pycnocline that were absent for the steady momentum run by t = 400 s and suggest the presence of internal waves behind the gravity current when momentum is variable.

A snapshot of salinity and velocity contours at t = 200 s show the near-field differences between steady and variable momentum simulations (Fig. 2a and b). Although the range of isohalines were the same for both runs, the pycnocline was more diffuse and nearer to the surface for steady momentum. Above and below a salinity of 20, flow was directed towards the right and left of the domain, respectively, at speeds of less than 0.4 ms^{-1}. Velocity vectors with opposing directions indicate the presence of vertical shear,

yet vertical velocities (< 0.1 ms^{-1}) and vorticity gradients were small for this run. Below a salinity of ~ 30, velocity vectors were even weaker at 0.06 ms^{-1}.

Stronger velocities and unstable salinity structure are the most striking features for the time-variable run (Fig. 2b). Increased positive and negative vertical velocities were observed adjacent to the unstable salinity, as well as large vorticities of 3.58 s^{-1}. Furthermore, the intensity of vorticity was greatest within the first 40 m and twice that observed in the nose of the plume (1.42 s^{-1}). Although vorticity is widely discussed, few papers provide actual quantities. Hence, the only comparison that could be made was to a laboratory experiment by Samothrakis and Cotel [2006], who found $\pm$ 2.5 s^{-1} for the head of the gravity currents induced by lock-exchange for Re $\sim$ 7500.

4.5. Stratification and mixing in the near-field

The non-dimensional gradient Richardson number, $\mathrm{Ri_g}$, is a widely used metric to evaluate the presence of turbulent mixing in a stratified fluid and is given by:

$$\mathrm{Ri_g} = \frac{-\mathrm{g}}{\rho_\mathrm{o}} \frac{\partial \rho}{\partial \mathrm{z}} \Big/ \frac{\partial \mathrm{U}^2}{\partial \mathrm{z}} \tag{10}$$

where $\partial\rho/\partial$z is the vertical density gradient and together with gravity and ρ_o, are the squared buoyancy frequency (N^2). Velocity shear (S^2) was determined from $\partial \mathrm{U}/\partial$z, the vertical velocity gradient. The canonical value of 0.25 delineates the transition from laminar to turbulent flow. However, an accepted range for the critical threshold, $\mathrm{Ri_{cr}}$ is from 0.25 to $\sim$ 0.40 [Thorpe, 2009]. For $\mathrm{Ri_g}$ between these values and $\sim$ 1 there would be sufficient release of energy to do mixing against gravity and larger-scale overturns are evident [Thompson, 1980].

It was instructive to separate, visually, contributions from the stabilizing buoyancy forces and destabilizing velocity shear (Fig. 2). For the steady momentum, S^2 was almost always smaller than N^2 and essentially zero once a quasi-equilibrium state was reached from 150 s onwards in the run (Fig. 2a). There were several exceptions early in the run, at 50 and 100 s for station 1 and 2, respectively, when velocity shear did exceed squared buoyancy frequency. These corresponded to Ri_g of between 0.1 to 0.5 (Fig. 2a), albeit with a lag between stations as the nose of the buoyant plume propagated past each mooring. However, the competition between shear and buoyancy was persistent in the near-field for variable momentum, with oscillating behavior back and forth between the dominant process (Fig. 2c and d). The longest period of stabilization (by stratification) occurred when momentum inputs decreased (from 100 to 150 s), but was short-lived once momentum increased again.

Much greater turbulent activity, seen by the many more occurrences of Ri_g of between 0.1 to 0.5, was evident for the variable momentum run (Fig. 2b). Moreover, the majority of these small-scale (KH) instabilities were located at stations 1 and 2. Instabilities at the larger Ri have not been examined (either experimentally or numerically) to the same extent as for when $Ri_{cr} \sim 0.25$, but even though mixing is less energetic at $Ri_{cr} > 2$ it is not negligible [Alexakis, 2009]. Analysis of velocity shear at deeper stations was several orders of magnitude smaller (essentially zero) than S^2 in the top 5 m and were insufficient to overcome the strong stable stratification.

Entrainment of relatively higher salinity water into the nose of the plume was characteristic for all simulations. However, stronger vorticity gradients and enhanced advection of the plume nose were only evident early in the time-variable momentum run. Figure 2

compared structure of the nose for the steady and variable momentum runs. Not only was the thickness of the nose smaller, entrained ambient water had relatively lower salinities and stratification was more stable in the peripheral region of the nose for the steady run. This was in stark contrast to the unstable salinity stratification observed within the core of the plume for the variable momentum. This, combined with upward vertical velocities (~ 0.2 ms^{-1}) that were twice as large as for steady inputs, resulted in stronger vorticity gradients. These snapshots were taken at t = 200 s, some 90 s after the second pulse of momentum occurred at 0 m. It seems that the influence of this variable input was two-fold. Not only was greater near-field mixing observed (Fig. 2b), but further downstream a faster, thicker plume propagated through the domain. Later snapshots revealed that by t = 350 s, the gravity current structure was retained for variable momentum. Unlike for steady momentum, which showed fewer similarities to a gravity current at the later time with the nose of the plume distorted and elongated.

5. Discussion

While the role of near-field mechanics is widely acknowledged to regulate the downstream plume [Garvine, 1999; Yankovsky et al., 2001], these mechanics have infrequently been included in numerical models and are not well understood. This idealized study of buoyant plumes, with Doubtful Sound for the framework, examined how the thin lens of buoyancy and energy is redistributed under buoyancy-only, buoyancy with steady and time-variable momentum forcing. From this idealized study questions arise such as what aspects of near-field mechanics regulate the far-field structure? And how does the adaptive model perform at simulating strongly shear-stratified coastal flows?

Horizontal gravity currents at a coastal scale

Momentum-driven gravity currents discharge as river plumes at the coastal margin. Buoyant plumes are event-driven features generated by the transient pulses of river discharge. Moreover, river flows are considered to have a greater influence than tidal oscillations composition and structure of the near-field and ultimately far-field plumes [Nash et al., 2009]. We have considered the purely surface advected plumes here, but since bottom connected plumes are also controlled by the variability of river flows [Kilcher and Nash, 2010] our findings are also applicable to the latter plume type.

From our numerical study, we found that near-field mixing is an order of magnitude greater when momentum is variable. Furthermore, greater vertical intrusions of brackish water occurred within the relatively short, but highly active mixing zone. Away from this region, faster propagation of the gravity current and greater advection and plume thickness highlighted the importance of the near-field mechanics. Without variable momentum inputs, a quasi-steady state was reached within several hundred meters in this idealized setting.

Length scales of active mixing, L_I (see introduction for definition), for the steady and variable momentum simulations were compared to typical length scales for the transition from jet to plume in Doubtful Sound. Mean values of L_I from the steady and variable model outputs were 5.4 and 24.6 m, respectively, based on N from station 1. Using external forcing data from Doubtful Sound, Q = 400 m^3s^{-1}, B = 100 m^4s^{-1} and M = 800 m^4s^{-1}, L_M was found to be $\sim$ 15 m. While it was encouraging that these metrics were of the same order of magnitude there are several caveats. First, the assumptions used to derive the relevant length scales oversimplify the mechanics of near-field mixing. Second,

model simulations are only 2D which limits the transfer of energy from large to smaller scales.

Energy transfers between kinetic and potential energy underpins mixing in density-stratified fluids [Thorpe, 1977]. The separation of potential energy into its available potential energy (APE) and background energy is a useful way of quantifying how much energy is available for mixing. A similar approach used by Winters et al. [1995] was initiated and although it was a largely prohibitive technique based on the number of cells in the Gerris domain, the outgoing fluxes of energy would misrepresent APE quantities in an open domain. Thus, an alternative evaluation based on differences between incoming and outgoing potential energy (PE) was ultimately used to determine quantities of APE stored for each run. PE was calculated for a uniform volume at the left and right boundaries at each time step using:

$$\mathrm{E_p} = \mathrm{g} \int_{\mathrm{V}} \rho \mathrm{z} \partial \mathrm{z}. \tag{11}$$

Figure 2 shows that APE is clearly greatest for the variable momentum run. There was no time when APE decreased to zero, indicating that there was always energy stored in the water column available for mixing, at least theoretically. Peltier and Caulfield [2003] consider lateral variations in density or statically unstable regions to exist when APE $>$ 0. Thus, unstable stratification persisted for the duration of the time-variable run. This is a major point of difference, since APE for the buoyancy only and steady momentum runs oscillated close to zero within 100 s and that although the water column was stratified it was stable beyond this time. While there is some decrease in APE for variable momentum over the same time scale (until 150 s), the second large momentum flux and subsequent

smaller pulses ensures that APE is non-zero for the remainder of the simulation. An order of magnitude difference in APE for the variable momentum simulations is a striking result. This concurs with the persistent shear instabilities in the near-field (Fig. 2c and d), yet the substantially higher APE is also likely to result from the feedback between these small-scale features and the propagating gravity current.

Although the field context for the idealized simulations was Doubtful Sound, transient pulses of river discharge that induce buoyant plumes dominate in many coastal environments. For systems that experience large seasonal signals, such as the spring freshet [O'Donnell, 1990], the most dramatic influence on ambient stratification will be associated with the initial pulse of freshwater. However, any subsequent inputs play an important role in maintaining the plume away from the estuary-coast boundary. Simulations indicate that variable forcing from the river boundary will lead to greater storage of potential energy in the plume region, which is available for conversion to kinetic energy further downstream such as seaward propagating internal waves [Nash and Moum, 2005].

An obvious omission from the simulations are the regular tidal oscillations at the downstream boundary, whereby enhanced stratification can occur due to tidal straining on the ebb and vice versa on the flood [Simpson et al., 1990]. The ebb/flood cycle and fortnightly tidal cycles would get superimposed on the temporal cycling of river discharges, which Halverson and Pawlowicz [2008] found to magnify tidal influences with increasing freshwater discharges in the Fraser River. Ultimately, forcing at the estuary-coast boundary will be a balance between event-driven river discharges and tidal stage. Regardless of the physical process responsible for a time-variable momentum flux to the coast, the associated response of enhanced near-field mixing is a thicker buoyant plume, captured here

numerically, that propagate seaward into the coastal zone where intermediate-to-far-field processes further modify the plume behavior.

Benefits of using an adaptive model

Two ways to evaluate the computing efficiency of a model is by data storage and simulation time. Table 2 shows the number of cells and corresponding file size for three simulations in this validation. Mean file sizes at time = 2.0 and 4.0 s were approximately 13 Mb and 30 Mb, respectively. Maximum file sizes were $\sim$ 80 Mb at the later time step (t = 10) for the highest Re of 10500, prior to the reflection of the gravity current at the end wall. Efficiency gains were evaluated by completing a simulation without adaptivity. A uniform mesh at quadtree level of 9 generated a grid to keep $\triangle$x $\sim 10^{-4}$, and with 6144×512 or $>$ 3 million cells computed at all time steps (essentially 2D DNS) the file size increased to 208 Mb. Thus, a saving of between 60 to $\sim$ 90 % in data storage was gained by using the adaptive mesh. A comparison of CPU time taken to complete 100 time steps for Re $\sim$ 10500 with and without adaptivity was made on the same processor (3.06 GHz CPU with 2 Gb Memory). It took between 1000 and 3000 s for this task with the adaptive mesh, but the duration was fixed at $\sim$ 15000 s for the full resolution grid. The average gain by using the adaptive mesh was $\sim$ 80% in CPU time. It was difficult to compare simulation times to other models since few of these details are documented, nevertheless, up to an order of magnitude savings in CPU time was made using the adaptive, hierarchical cell structure in Gerris.

Substantial computational savings by using a model with AMR were highlighted by the lock-exchange validation, with gains of up to an order of magnitude in time and data storage. This particular problem initially has zero flow or density structure making it

well-suited to taking advantage of the adaptive quadtree and octree structures in Gerris. This, coupled with the scale of the problem – 0.2×2.4 m – meant that simulations with sufficient cell refinement were able to resolve the full temperature spectrum as was done by Härtel et al. [2000].

However, the same is not true for gravity current simulations at the coastal scale. An adaptive run for steady momentum was performed to compare the static quadtree to AMR. For the static grid, 5000 time steps, or about 295 s of simulation time took approximately 92 hours of CPU time. This was reduced to 58.5 hours with adaptivity. It took a total of 4 days of CPU time, compared to > 6.5 days, with AMR for the horizontal gravity current to propagate along the length of the domain. Quadtree levels ranged from 6 to 9 as per the static grid. Initially, this range was motivated by making an equivalent comparison to the static grid, however, the presence of ambient stratification in the fjord (or coast) means that the choice of refinement levels cannot be on an ad hoc basis. Decreasing the quadtree level from 6 to 5 meant that the initial cell resolution was $50/2^5$ or ~ 1.56 m. This leads to initial stratification being under-resolved in this coastal problem. Rickard et al. [2009] found a similar result, confirming that adaptivity cannot compensate for initially unresolved scales implied by the boundaries or initial stratification.

Computing power limits the scales able to be resolved, raising the question about accuracy of the MILES sub-grid-scale (SGS) turbulence closure scheme that we used. The parameter space for the three different runs was constant; dimensional viscosity was $\nu = 5 \times 10^{-5} \mathrm{m}^2\mathrm{s}^{-1}$ and based on a length = 50 m and initial velocity of 1 ms^{-1} gives a Re of 1×10^6. If we consider the criteria outlined by Härtel et al. [1997] for achieving a decay of 3 to 4 orders of magnitude in temperature, then $\triangle$x should be $\sim 3.77 \times 10^{-4}$ for

this Re number. Gerris is resolving scales (for the plume problem) down to 30 mm cell width/height. A $\triangle$x of 30 mm is, however, several orders larger than the 0.37 mm cell size required to resolve the full temperature spectrum.

The use of the MILES approach has only been used in non-stratified turbulent flows [Grinstein and Fureby, 2002], including the validation done for Gerris [Popinet et al, 2004]. So, what sense can be made of the turbulent behavior from these simulations in strongly stratified systems? Ultimately, a detailed study comparing several SGS turbulent closure schemes for the Gerris model is required. But, good agreement between the MILES and Smagorinksy models, an alternative SGS turbulent closure scheme that has been used in stratified flows [Ozgokmen et al., 2007], for the decay of isotropic turbulence was shown by [Okong'O et al., 2000]. They found that SGS eddy viscosity was less than 10 % of the molecular viscosity and that MILES was effectively LES with molecular viscosity. Thus, it is highly likely that the turbulent decay and transfer of energy to higher frequencies was restricted more by simulations being 2D than the SGS scheme employed.

It is clear that the choice and optimization of the adaptivity criteria is crucial to obtain the gains in efficiency which can justify the increased complexity of adaptive methods (in this respect one can consider that a decrease of one order of magnitude at least is necessary). How to find these optimal criteria is still an open question. While the simple ad hoc criteria we used worked well in the case of the laboratory-scale experiment, their generalization to the more complex, turbulent field-scale problem is not simple and warrants further study. The relationship between local spatial resolution and subgrid-scale turbulence models could be of particular interest in this respect. Indeed, it is well-known that turbulence models can be tuned to work well in some conditions (e.g. isotropic

turbulence) but not in others. This could be used to define adaptivity criteria which would use a coarse mesh where the local subgrid-scale processes are known to be accurately modeled and a finer mesh elsewhere. With our current vorticity criterion, these areas of e.g. isotropic turbulence will likely be resolved at the finest resolution allowed, thus not realizing the potentially-large gains in mesh resolution.

Future work will have a similar focus, but will need to encompass both baroclinic and barotropic variability at scales greater than investigated here, i.e. from $\sim$ 100 m up to several kms (at least for plumes with moderate river discharges) and will also need to be three-dimensional. At this larger scale, the balance between subgrid-scale turbulence schemes and cell resolution by adaptivity will need to be evaluated to ensure that simulations capture the relevant energy scales when plumes discharge into the coastal zone (i.e. energy cascade to internal waves, turbulent mixing and smaller).

6. Conclusions

Understanding how buoyancy and energy are redistributed in the near-field buoyant plume was examined using Gerris, an adaptive Navier-Stokes solver.

- We have successfully validated the use of the Boussinesq approximation in Gerris using the classical lock-exchange problem. We have shown that this adaptive model can capture the multiscale nature range of processes for L $\sim$ 100 m. The model reproduced the gravity currents for both laminar and turbulent flows and were comparable to other non-hydrostatic numerical codes. Further, simulations for slip and no-slip conditions converged to the theoretical limit by Benjamin [1968], which remains a benchmark for the lock-exchange problem. The high Re numbers simulated by Gerris are some of the

highest captured by a numerical model; this was possible due to the computationally efficient AMR employed. This validation of buoyancy-driven flow gave us confidence in subsequent simulations of field-scale buoyant plumes.

• Two-dimensional simulations examined the response of the buoyant gravity current under zero, steady and variable momentum fluxes from the upstream boundary. From our study of an idealized plume we found that advection was 30 % greater for plumes forced with steady momentum (than buoyancy only). After an initial displacement of the pycnocline, quasi-steady state is reached by the buoyant plume within several hundred meters without additional momentum at the upstream boundary.

• Time-variable momentum inputs result in a substantially thicker gravity current as h_f of the nose increased from 5 to 7 m. Greater near-field mixing was also evident for the variable run with $\mathrm{Ri}_{\mathrm{cr}}$ exceeded many more times in the first 100 m of the discharge point. Ongoing competition between shear and buoyancy occurred after both the initial and subsequent momentum flux. Simulations indicate that variable inputs of momentum can lead to greater storage of available potential energy in the near-field region and were up to an order of magnitude greater than for steady momentum. Transient flows play an important role in mixing and plume structure in the near-field, while any subsequent inputs of momentum could help to maintain (along with other intermediate and far-field processes) the plume away from the estuary-coast boundary.

Acknowledgments. This work was funded by the Foundation for Research, Science, and Technology, New Zealand, Sustainable Aquaculture programme and Ministry of Research, Science and Technology, New Zealand Capability Funding. The suggestions of two anonymous reviewers greatly improved this manuscript.

References

Alexakis, A., 2009. Stratified shear flow instabilities at large Richardson numbers *Physics of Fluids* 21, 054108, doi:10.1063/1.3147934.

Benjamin, T. B., 1968. Gravity currents and related phenomena.*Journal of Fluid Mechanics,* 31, 209-248.

Berntsen, J., Xing, J., Alendal, G., 2006. Assessment of non-hydrostatic ocean models using laboratory scale problems. *Continental Shelf Research,* 26, 1433-1447.

Bourgault, D., Kelley, D. E. 2004. A laterally averaged nonhydrostatic ocean model, *Journal of Atmospheric and Oceanic Technology,* 21, 1910-1924.

Burchard, H. 2002. Applied turbulence modelling in marine waters. Series: Lecture Notes in Earth Sciences, Vol. 100, Springer. 215p.

. Chao, S. Y., Boicourt, W.C., 1986. Onset of estuarine plumes. *Journal of Physical Oceanography,* 16, 2137-2149.

Fischer, H. B., List, E. J., Imberger, J., Koh, R. C. Y., Brooks, N. H. 1979. Mixing in Inland and Coastal Waters, Academic Press, New York, 483 pp.

Fringer, O. B., Gerritsen, M., Street, R. L., 2006. An unstructured-grid, finite-volume, nonhydrostatic, parallel coastal-ocean simulator, *Ocean Modelling,* 14 (3-4), 139-278.

Fong, D.A., Geyer, W.R., 2002. The alongshore transport of freshwater in a surface-trapped river plume. *Journal of Physical Oceanography,* 32 (3), 957-972.

Garvine, R.W., 1974. Dynamics of small-scale oceanic fronts. *Journal of Physical Oceanography,* 4, 557- 569.

Garvine, R.W., 1987. Estuary plumes and fronts in shelf waters: A layer model. *Journal of Physical Oceanography,* 17, 1877-1896.

Garvine, R. W., 1999. Penetration of buoyant coastal discharge onto the continental shelf. *Journal of Physical Oceanography,* 29, 18921909.

Gibbs, M.T., Bowman, W. J., Dietrich, D.E., 2000. Maintenance of Near-Surface Stratification in Doubtful Sound, a New Zealand Fjord. *Estuarine, Coastal and Shelf Science*, 51(6), 683-704.

Grinstein, F. F. Fureby, C. 2002. Recent progress on MILES for high Reynolds number flows, *Journal of Fluids Engineering*, 124(4), 848-862.

Halverson, M. J., Pawlowicz, R. 2008. Estuarine forcing of a river plume by river flow and tides. *Journal of Geophysical Research,* 113, C09033, doi:10.1029/2008JC004844.

Härtel, C., Kleiser, L., Michaud, M., Stein, C. F. 1997. A direct numerical simulation approach to the study of intrusion fronts. *Journal Engineering Maths*, 32, 103-120.

Härtel, C., Meiburg, E., Necker, F., 2000. Analysis and direct numerical simulation of the flow at a gravity-current head. Part 1. Flow topology and front speed for slip and no-slip boundaries. *Journal of Fluid Mechanics,* 418, 189-212.

Hearn, C. J. 2007. The Dynamics of coastal models. Cambridge University Press. 488p.

Hickey, B., Geier, S., Kachel, N., MacFadyen, A. 2005. A bi-directional river plume: The Columbia in summer *Continental Shelf Research,* 25 (14), 1631-1656. doi: 10.1016/j.csr.2005.04.010

Horner-Devine, A.R. 2009. The bulge circulation in the Columbia River plume. *Continental Shelf Research,* 29 (1), 234-251.

Itsweire, E. C., Koseff, J., Briggs, D. A., Ferziger, J. H. 1993. Turbulence in stratified shear flows: Implications for interpreting shear-induced mixing in the ocean, *Journal of Physical Oceanography,* 23, 1508 1522.

Jirka, G.H. 2004. Integral model for turbulent buoyant jets in unbounded stratified flows. 1: The single round jet. *Environmental Fluid Mechanics,* 4, 1-56.

Jones, G.M., Nash, J.D., Doneker, R.L., Jinka, G.H. 2007. Buoyant surface discharge into water bodies. I: Flow classification and prediction methodology. *Journal of Hydraulic Engineering,* 133(9): 1010-1020.

Kilcher, L. F. Nash, J. D. 2010. Structure and dynamics of the Columbia River tidal plume front.*Journal of Geophysical Research,* 115, C05S90, doi:10.1029/2009JC006066.

Kourafalou, V.H., Oey, L.-Y., Wang, J.D., Lee, T.N. 1996. The fate of river discharge on the continental shelf 1. Modeling the river plume and the inner shelf coastal current. *Journal of Geophysical Research*, 101 (C2), 3415-3434.

Luketina, D., Imberger, J. 1987. Characteristics of a surface buoyant jet. *Journal of Geophysical Research,* 92(C5), 5435-5447.

Luketina, D., Imberger, J. 1989. Turbulence and entrainment in a buoyant surface plume. *Journal of Geophysical Research*, 94(C9), 12619-12636.

MacCready, P., Banas, N.S., Hickey, B.M., Dever, E.P., Liu, Y., 2008. A model study of tide- and wind-induced mixing in the Columbia River estuary and plume. *Continental Shelf Research,* 29(1), 278-291. doi:10.1016/j.csr.2008.03.015.

MacDonald, D. G., and Geyer, W.R. 2004. Turbulent energy production and entrainment at a highly stratified estuarine front. *Journal of Geophysical Research*, 109, C05004, doi:10.1029/2003JC002094.

McDougall, T. J., Jackett, D. R., Wright, D. G., Feistel, R. 2003. Accurate and computationally efficient algorithms for potential temperature and density of seawater. *Journal of Atmospheric and Oceanic technology*, 20, 730-741.

Marino, B., Thomas, L., Linden, P., 2005. The front condition for gravity currents. *Journal of Fluid Mechanics,* 536, 49-78.

Marshall, J., Hill, C., Perelman, L., Adcroft, A., 1997. Hydrostatic, quasi-hydrostatic, and nonhydrostatic ocean modeling. *Journal of Geophysical Research,* 102 (C3), 5733-5752.

Maxworthy, T., Lelich, J., Simpson, J.E., Meiburg, E.H. 2002. The propagation of a gravity current into a linearly stratified fluid. *Journal of Fluid Mechanics,* 453, 371-394.

Nash, J.D., Kilcher, L. F., Moum, J.N., 2009. The structure and composition of a strongly-stratified, tidally-pulsed river plume. *Journal of Geophysical Research, in press.*

Nash, J.D., Moum, J.N., 2005. River plumes as a source of large-amplitude internal waves in the coastal ocean. *Nature*, 437 (7057), 400-403. doi: 10.1038/nature03936

Nikiema, O., Devenona, J.L., Baklouti, M. 2007. Numerical modeling of the Amazon River plume. *Continental Shelf Research,* 27(7), 873-899. doi:10.1016/j.csr.2006.12.004

O'Donnell, J. 1990. The formation and fate of a river plume: a numerical model. *Journal of Physical Oceanography,* 20(4), 551-569.

O'Donnell, J., Ackleson, S. G., Levine, E. 2008. On the spatial scales of a river plume. *Journal of Geophysical Research,* 113, C04017, doi:10.1029/2007JC004440.

Okong'O, N., Knight, D. D., Zhou, G. 2000. Large Eddy Simulations Using an Unstructured Grid Compressible Navier–Stokes Algorithm. *Computational Fluid Dynamics*, 13 (4), 303-326.

Ooi, S. K., Constantinescu, G., Weber, L. J. 2007. 2D Large-Eddy Simulation of Lock-Exchange Gravity Current Flows at High Grashof Numbers. *Journal of Hydraulic Engineering,* 133 (9), 10371047.

Orton, P. M., Jay, D. A. 2005. Observations at the tidal plume front of a high volume river outflow. Geophys. Res. Lett. 32, L11605 doi:10.1029/2005GL02237.

Ozgokmen, T., Chassignet, E., 2002. Dynamics of two-dimensional turbulent bottom gravity currents. *Journal of Physical Oceanography,* 32, 1460-1478.

Ozgokmen, T., Iliescu, T., Fischer, P., Srinivasan, A., Duan, J., , 2007. Large eddy simulation of stratified mixing in two-dimensional dam-break problem in a rectangular enclosed domain. *Ocean Modelling* 16, 106-140.

Pain C.C., Piggott M.D., Goddard A.J.H., Fang, F., Gorman, G.J., Marshall, D.P., Eaton, M.D., Power, P.W., de Oliveira, C.R.E. (2005). Three-dimensional unstructured mesh ocean modelling, *Ocean Modelling,* 10, 5-33, doi:10.1016/j.ocemod.2004.07.005.

Peltier, W. R., Caulfield, C. P. 2003. Mixing Efficiency in stratified shear flows. *Annual Review Fluid Mechanics,*, 35, 135-167. doi: 10.1146/annurev.fluid.35.101101.161144.

Popinet, S., 2003. Gerris: A tree-based adaptive solver for the incompressible Euler equations in complex geometries. *Journal of Computational Physics,* 190 (2), 572-600.

Popinet, S., 2006. The Gerris Flow Solver. http://gfs.sourceforge.net.

Popinet, S., 2009. An accurate adaptive solver for surface-tension-driven interfacial flows. *Journal of Computational Physics*, 228, 58385866.

Popinet, S., Rickard, G., 2007. A tree-based solver for adaptive ocean modelling. *Ocean Modelling,* 16, 224-249

Popinet, S., Smith, M., Stevens, C. 2004. Experimental and numerical study of the turbulence characteristics of air flow around a research vessel. *Journal of Atmospheric and Oceanic Technology,* 21(10), 1574-1589.

Rickard, G., O'Callaghan, J., Popinet, S. 2009. Numerical simulations of internal solitary waves interacting with uniform slopes using an adaptive model. *Ocean Modelling,* 30, 16-28, doi:10.1016/j.ocemod.2009.05.008.

Samothrakis, P., Cotel, A. J. 2006. Propagation of a gravity current in a two-layer stratified environment *Journal of Geophysical Research,* 111, C01012, doi:10.1029/2005JC003125.

Shin, J.O., Dalziel, S.B., Linden, P.F., 2004. Gravity currents produced by lock exchange. *Journal of Fluid Mechanics,* 521, 1-34.

Simpson, J.H., Brown, J., Matthews, J. and Allen, G. 1990. Tidal straining, density currents, and stirring in the control of estuarine stratification. *Estuaries,* 13(2):125–132.

Simpson, J. E. 1997. Gravity currents in the environment and the laboratory. 2nd edn. Cambridge University Press.

Simpson, J., Britter, R., 1979. The dynamics of the head of a gravity current advancing over a horizontal surface. *Journal of Fluid Mechanics,* 94, 477- 495.

Smagorinsky, J., 1963. General circulation experiments with the primitive equations. *Monthly Weather Review*, 91, 99164.

Stashchuk, N., Vlasenko, V., 2009. Generation of internal waves by a supercritical plume. *Journal of Geophysical Research,* 114, C01004, doi:10.1029/2008/JC004851.

Thompson, R.O.R.Y., 1980. Efficiency of conversion of kinetic energy to potential energy by a breaking internal gravity wave. *Journal of Geophysical Research,* 85, C11, 6631-6635.

Thorpe S. A., 1977. Turbulence and mixing in a Scottish Loch. *Philosophical Transactions Royal Society*, 286A, 125181.

Thorpe S. A., Liu, Z., 2009. Marginal Instability? *Journal of Physical Oceanography*, 39 (9), 2373-2381.

Wadzuk, B. M., Hodges, B. R. 2004. Hydrostatic and Non-hydrostatic Internal Wave Models. CRWR Online Report 04-09 Available from: www.crwr.utexas.edu. Accessed March 18, 2009.

Wang, B., Fringer, O.B., Giddings, S.N., Fong,D.A. 2008. High-resolution simulations of a macrotidal estuary using SUNTANS. *Ocean Modelling,* 26, 60-85, doi:10.1016/j.ocemod.2008.08.006.

Whitney, M. M., Garvine, R.W., 2006. Simulating the Delaware Bay buoyant outflow: Comparison with observations. *Journal of Physical Oceanography,* 36(1), 3-21.

Winters, K.B., Lombard, P.N., Riley, J.J., D'Asaro, E.A. 1995. Available potential energy and mixing in density-stratified fluids. *Journal of Fluid Mechanics,* 289, 115-128.

Yankovsky, A.E. Hickey, B.M. Münchow, A.K. 2001. Impact of variable inflow on the dynamics of a coastal buoyant plume. *Journal of Geophysical Research,* 106 (C9), 19809-19824.

Table 1. Summary of Re_f number, viscosity and Gr number for the lock-exchange test case.

$Re_f(u_f h_f/\nu)$	$\hat{\nu}$	ν ($m^2 s^{-1}$)	Gr $(u_b.h/\nu)^2$
~ 300	1.78×10^{-4}	8.94×10^{-4}	3.13×10^5
~ 2600	1.78×10^{-5}	8.94×10^{-5}	3.13×10^7
~ 10500	4.0×10^{-6}	2.0×10^{-5}	6.25×10^8

Table 2. Cell and file size for different Re numbers for no-slip boundary conditions.

Re_f	Cell numbers		File Size (Mb)	
	t(s) = 2.0	4.0	t(s) = 2.0	4.0
300 (adaptivity)	235000	370000	16	36
2600 (adaptivity)	185000	405000	12	27
10500 (adaptivity)	165000	378000	11	25
10500 (No adaptivity)	4194300	4194300	208	208

Figure 1: Lock-exchange flow in a channel of length 12 L, with a dimensional length of L = 0.2 m, giving a domain of 0.2 × 2.4 m as per experiments of Maxworthy et al. [2002].

Figure 2: Development of gravity current for Re_f numbers of (a) 300, (b) 2600, (c) 10500 at time = 11 s with no-slip boundary conditions. Bulk Re are between 3 to 4 times higher than Re_f. Note that the y-axis has a 1:2 ratio to improve clarity of the small-scale instabilities.

Figure 3: Normalized time versus horizontal position of gravity current normalized by domain length for Re_f = 300 (squares), 2600 (triangles), and 10500 (circles) with no-slip conditions (triangle). Filled circles represent Re = 10500 with a slip boundary condition.

Figure 4: Snapshot of head of gravity current at Re_f = 10500 for (a) slip and (b) no-slip boundary conditions at time = 6.2 s. The dimensional length scale in the y-direction was 0.2 m.

Figure 5: Vorticity response of lock-exchange with contours ranging from ± 10 s^{-1} with at 1 s^{-1} intervals (top) and corresponding adaptive mesh grid (bottom) showing quad-tree levels from 5 to 8. Note that the maximum quad-tree level was 9 but reduced to 8 for clarity. These data correspond to Fig. 4b.

Figure 6: Froude number of the front of the gravity current, Fr, as a function of the Re number. Open circles and open squares correspond to present 2D high-resolution simulations with no-slip and slip boundary conditions. Closed circles and triangles correspond to simulations using BOM and MIT in Berntsen et al. [2006]. Asterisks correspond to no-slip DNS simulations of Härtel et al. [1997]. Slip DNS simulations by Härtel et al. [2000] were not included since these used a Gr-Fr diagram, but did have faster speeds at all Gr as seen here.

Figure 7: Buoyancy only gravity current in highly stratified water column at (a) start of simulation, (b) time = 200 s and (c) 400 s. Note that the y-axis has a 1:2 ratio for better clarity and only the top 30 m of the water column are included. Time series in later plots were obtained at 25 and 75 m along the domain and identified by the vertical lines in (a). Note that the 200 m 'mooring' is positioned immediately to the right of the domain in (a).

Figure 8: Boundary conditions for steady (dashed) and variable momentum (solid) inputs. N.B. These line patterns differ from outputs of corresponding runs for clarity.

Figure 9: Steady and variable momentum inputs at highly stratified water column with (a) initial conditions for both cases, steady momentum at (b) t = 200 s and (d) t = 400 s and variable momentum at (c) t = 200 s and (e) 400 s. Note that the y-axis has a 1:2 ratio for better clarity and only the top 30 m of the water column are included. The horizontal and vertical scales for these runs are shown in Fig. 7.

Figure 10: Plume thickness, h_f for the buoyancy only (solid), steady momentum (dot-dashed) and variable momentum (dotted) runs, where h_f is specified in Fig. 2b.

Figure 11: Isohalines with velocity vectors at time = 200 sec for (a) steady and (b) variable momentum. The vertical line is 25 m from the left boundary. Vector lengths are equivalent in (a) and (b).

Figure 12: Time series of N^2 (dashed) and S^2 (solid) at 2.5 m from the top of the domain for (a) station 1 and (b) station 2 for steady momentum and (c) station 1 and (d) station 2 for variable momentum.

Figure 13: Time series of Ri_g in the top 5 m of the water column for (a) steady and (b) variable momentum simulations. $Ri_{cr} = 0.25$ is the given by the dotted line. Stations 1, 2 and 3 are represented by the pluses, filled squares and open circles, respectively.

Figure 14: Contours of salinity (color) with dark blue = 5 and red = 34.7, vorticity contours in the x-z plane at 0.18 s^{-1} intervals and velocity vectors scaled proportional to the maximum speed of 2 ms^{-1}. All snapshots are at time = 200 s, for steady (top) and variable (bottom) momentum inputs. Vertical lines are 150 and 200 m from the left boundary.

Figure 15: Stored or available potential energy (APE) for the buoyancy only (solid), steady (dot-dashed) and variable momentum (dotted) simulations.

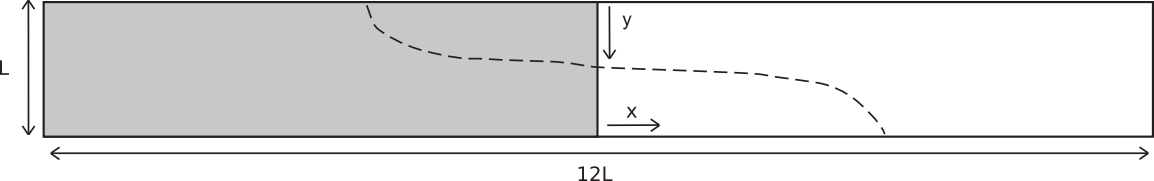
L
y
x
12L

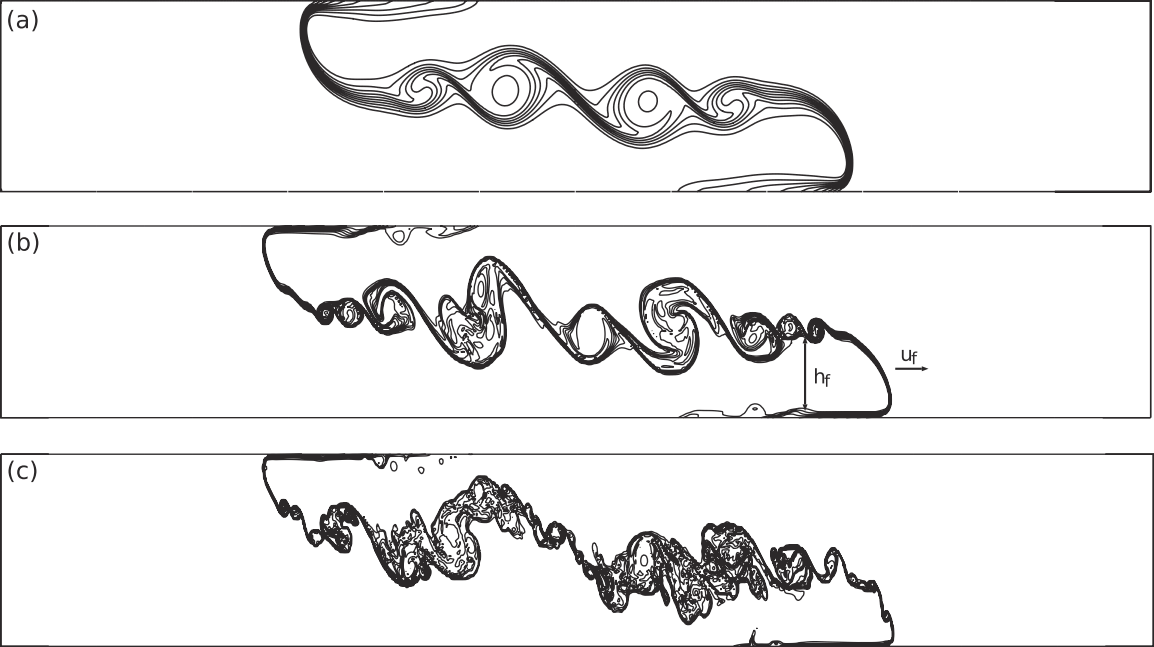
(a)
(b)
u_f
h_f
(c)

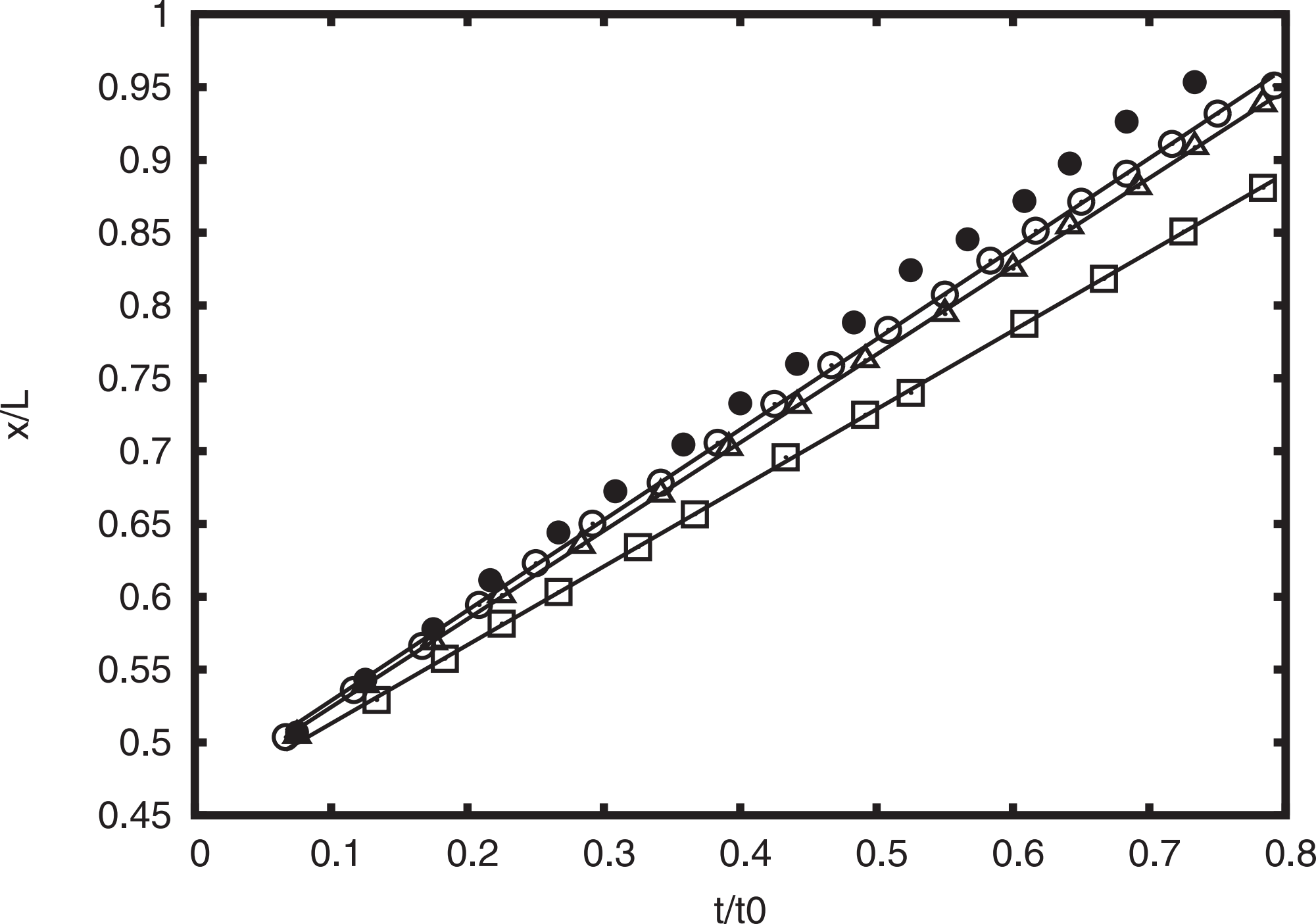
1
0.95
0.9
0.85
0.8
0.75
0.7
0.65
0.6
0.55
0.5
0.45
x/L
0
0.1
0.2
0.3
0.4
0.5
0.6
0.7
0.8
t/t0

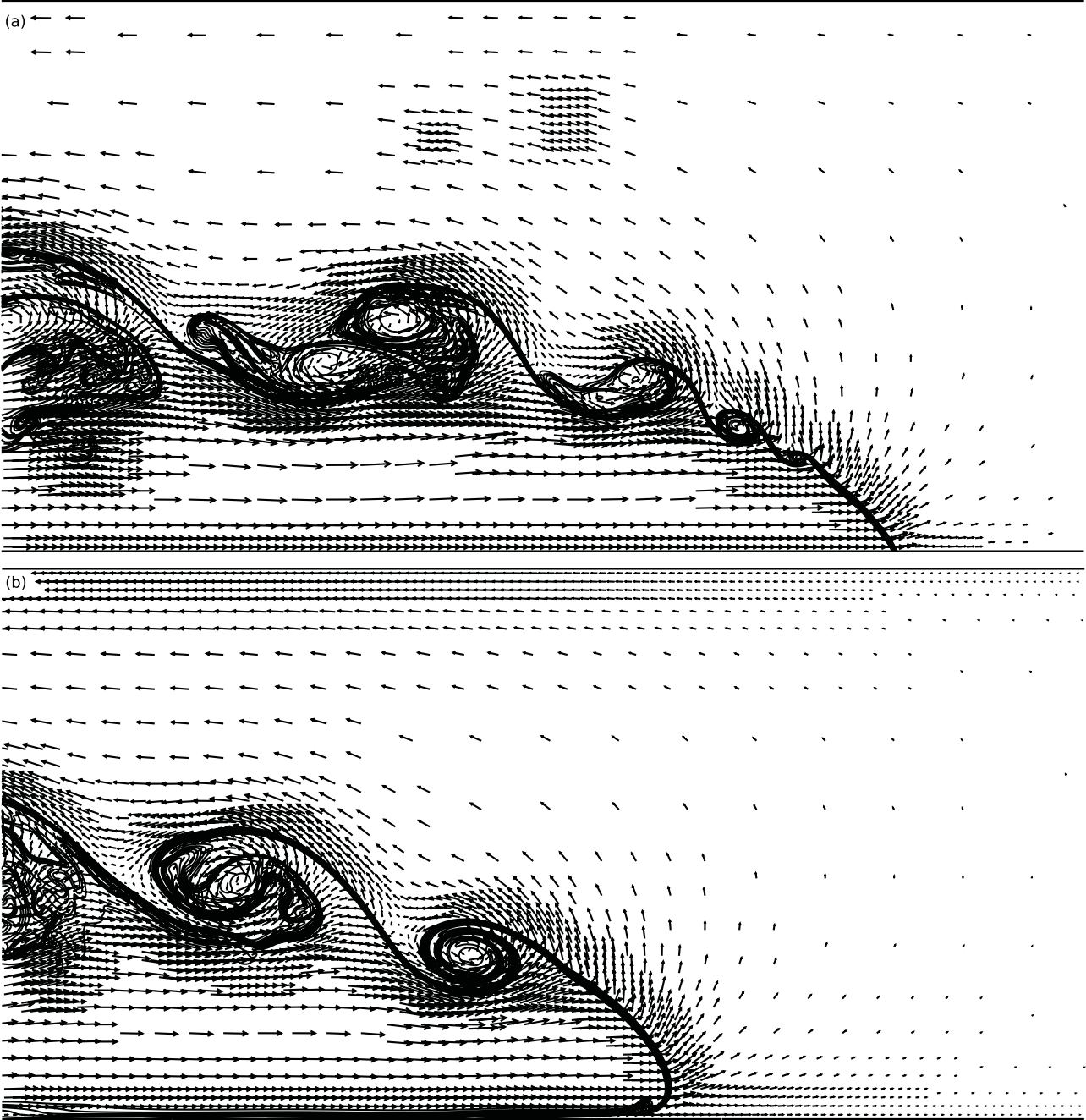
(a)
(b)

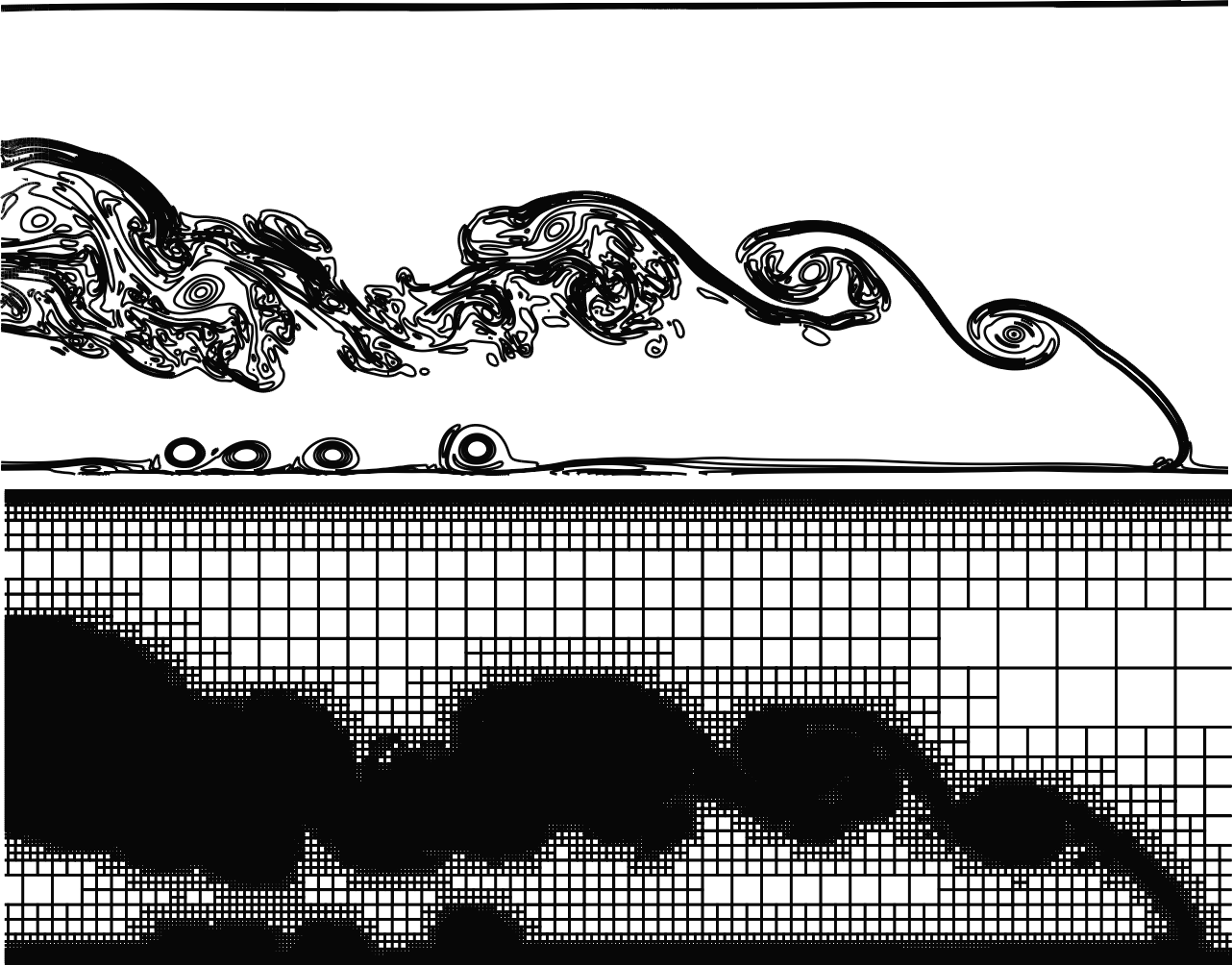

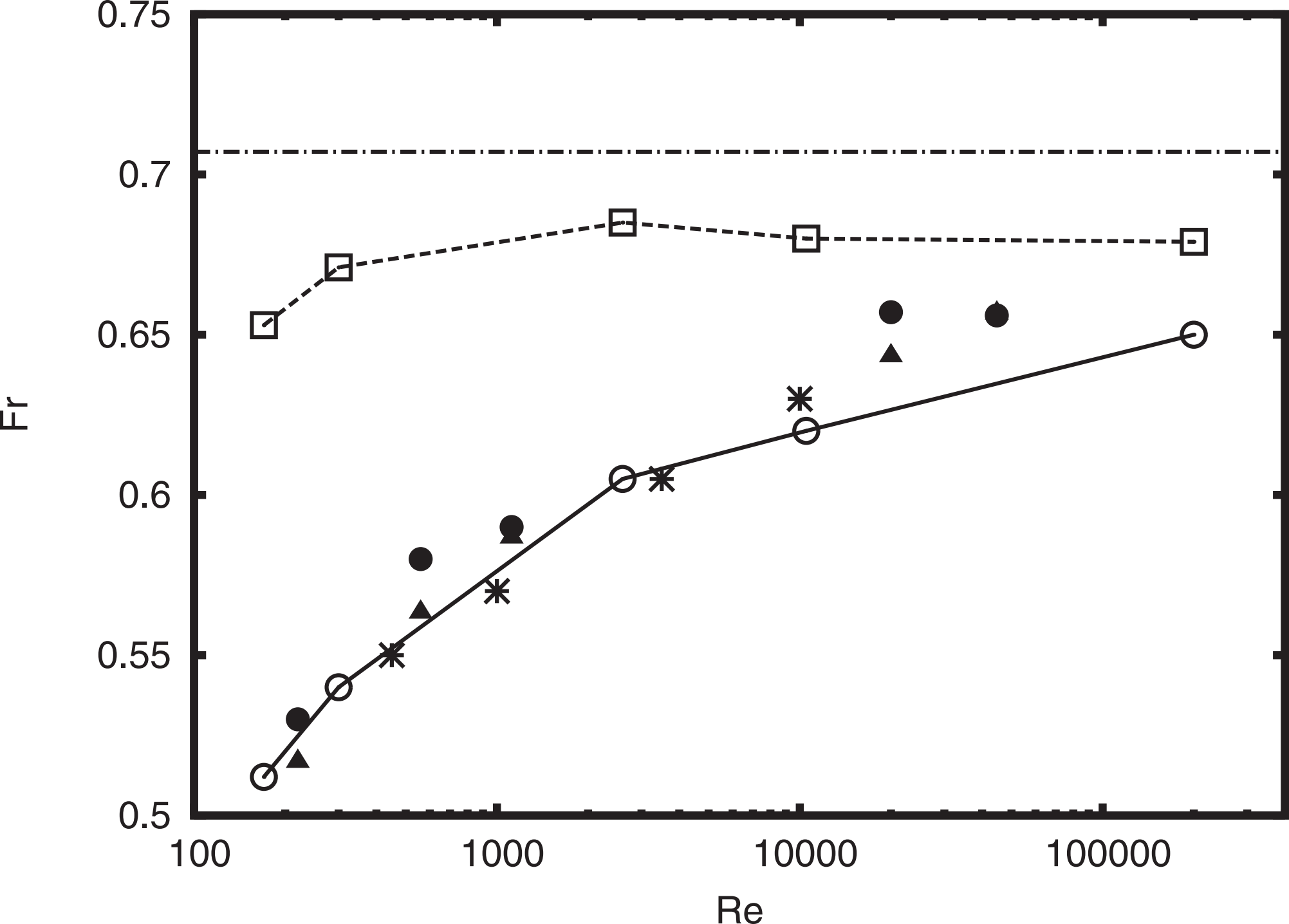
0.75
0.7
0.65
0.6
0.55
0.5
Fr
100
1000
10000
100000
Re

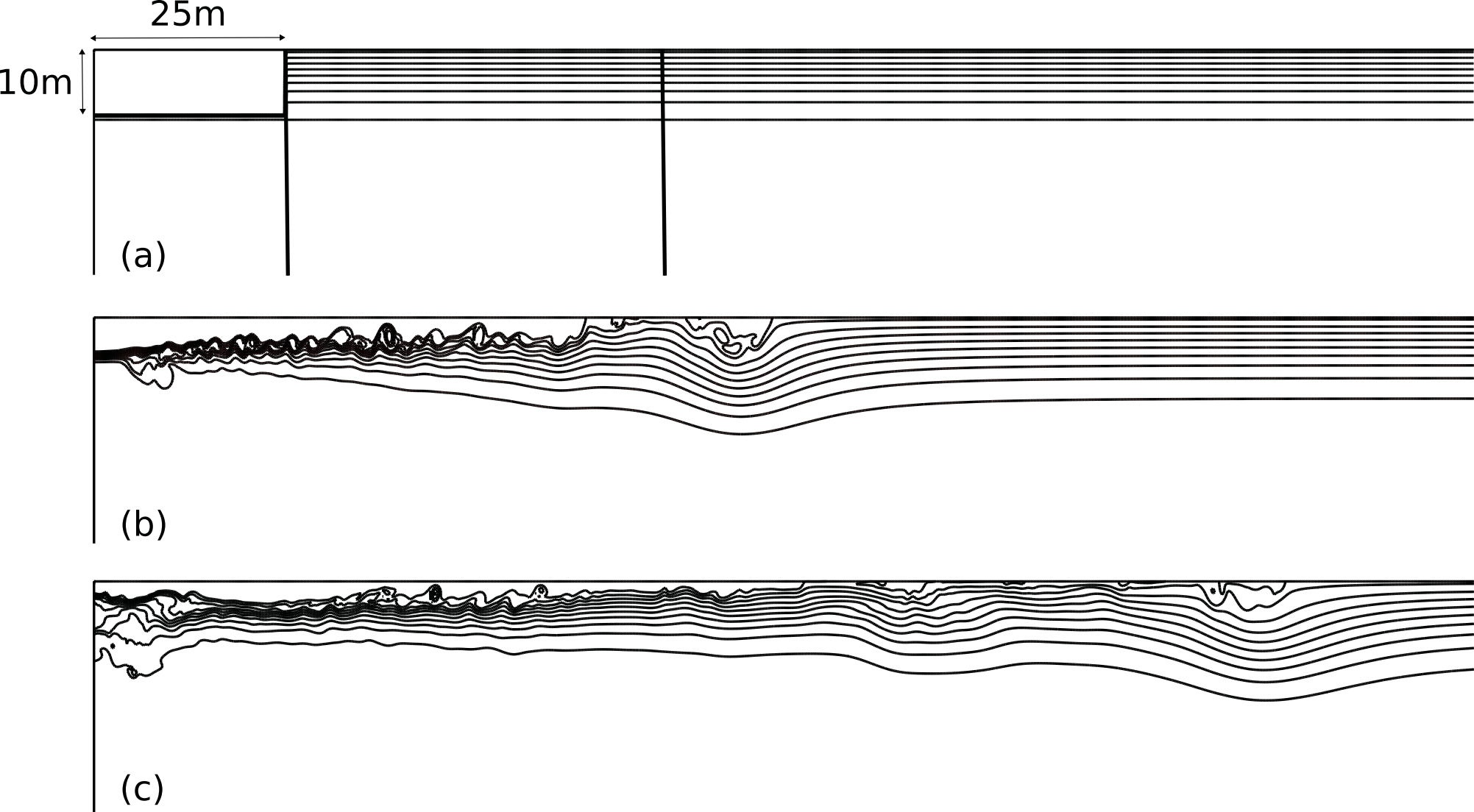
25m
10m
(a)
(b)
(c)

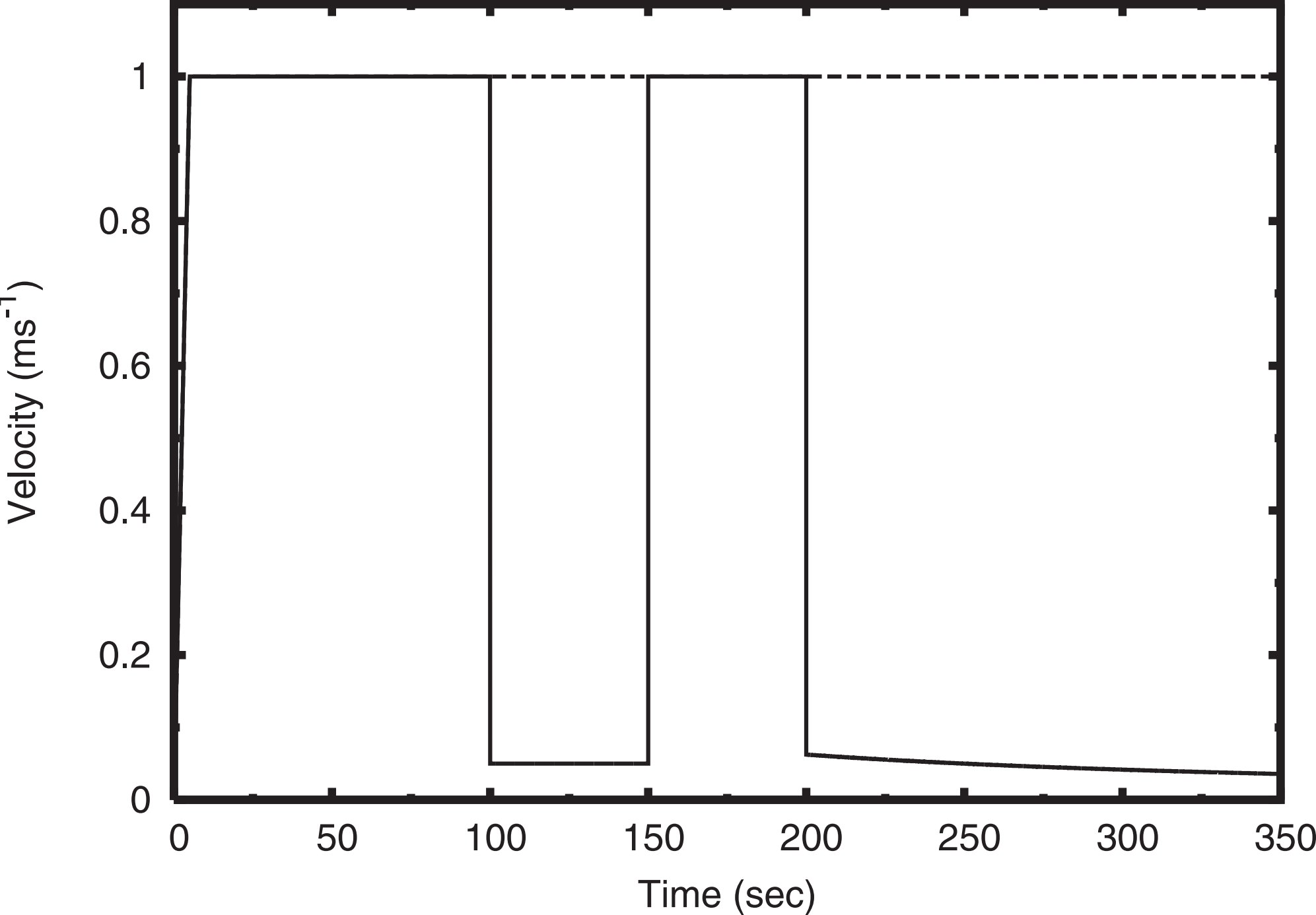
1
0.8
0.6
0.4
0.2
0
Velocity (ms-1)
0
50
100
150
200
250
300
350
Time (sec)

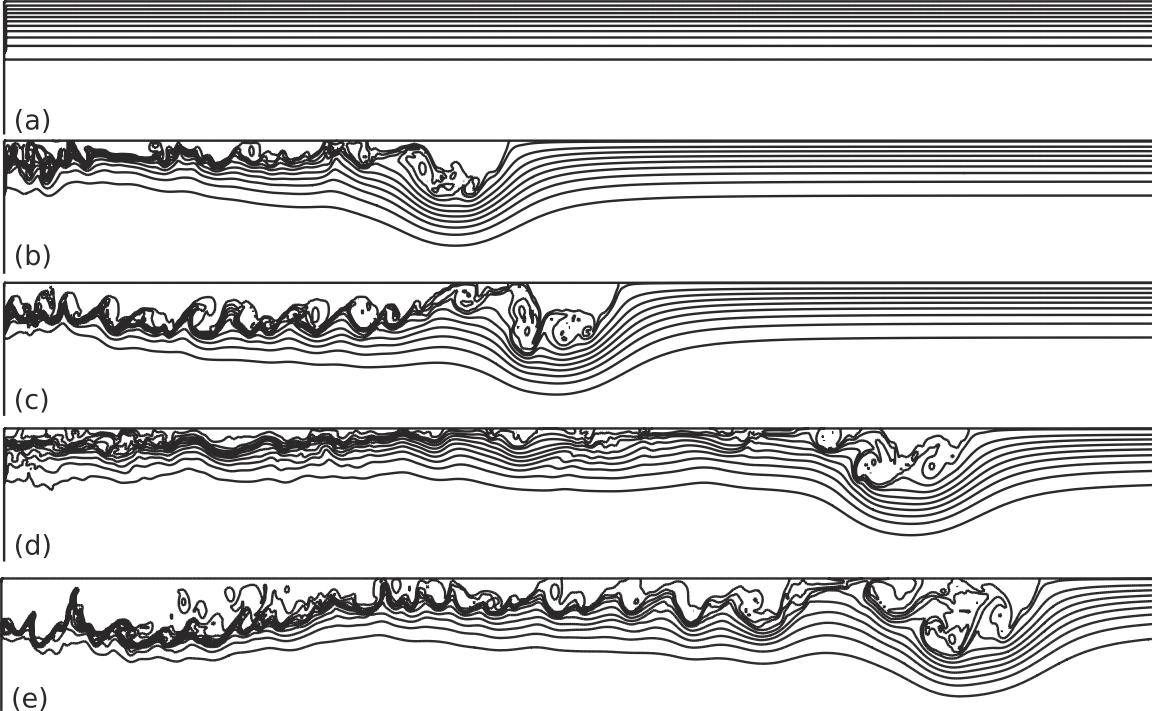
(a)
(b)
(c)
(d)
(e)

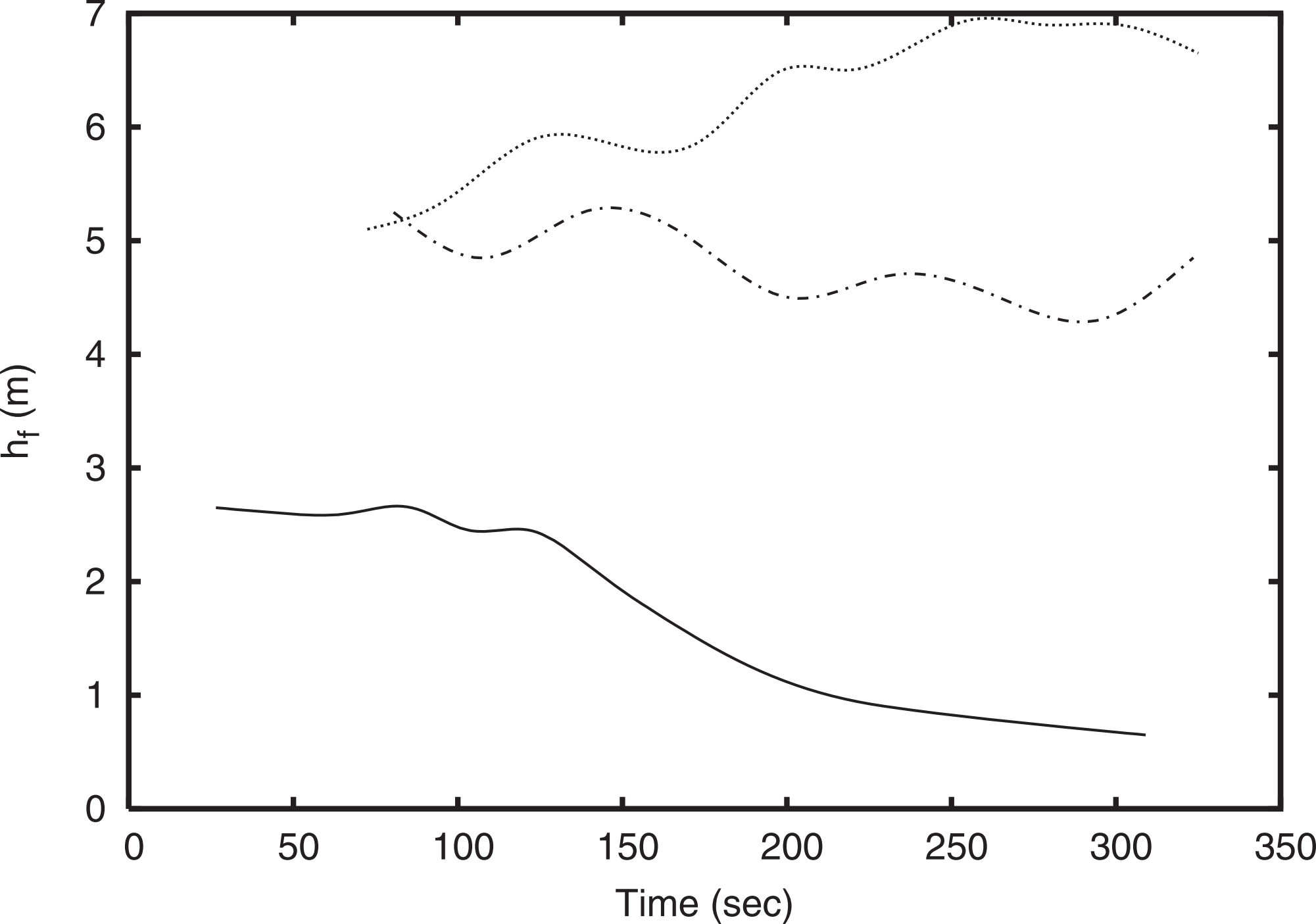
7
6
5
4
3
2
1
0
h_f (m)
0
50
100
150
200
250
300
350
Time (sec)

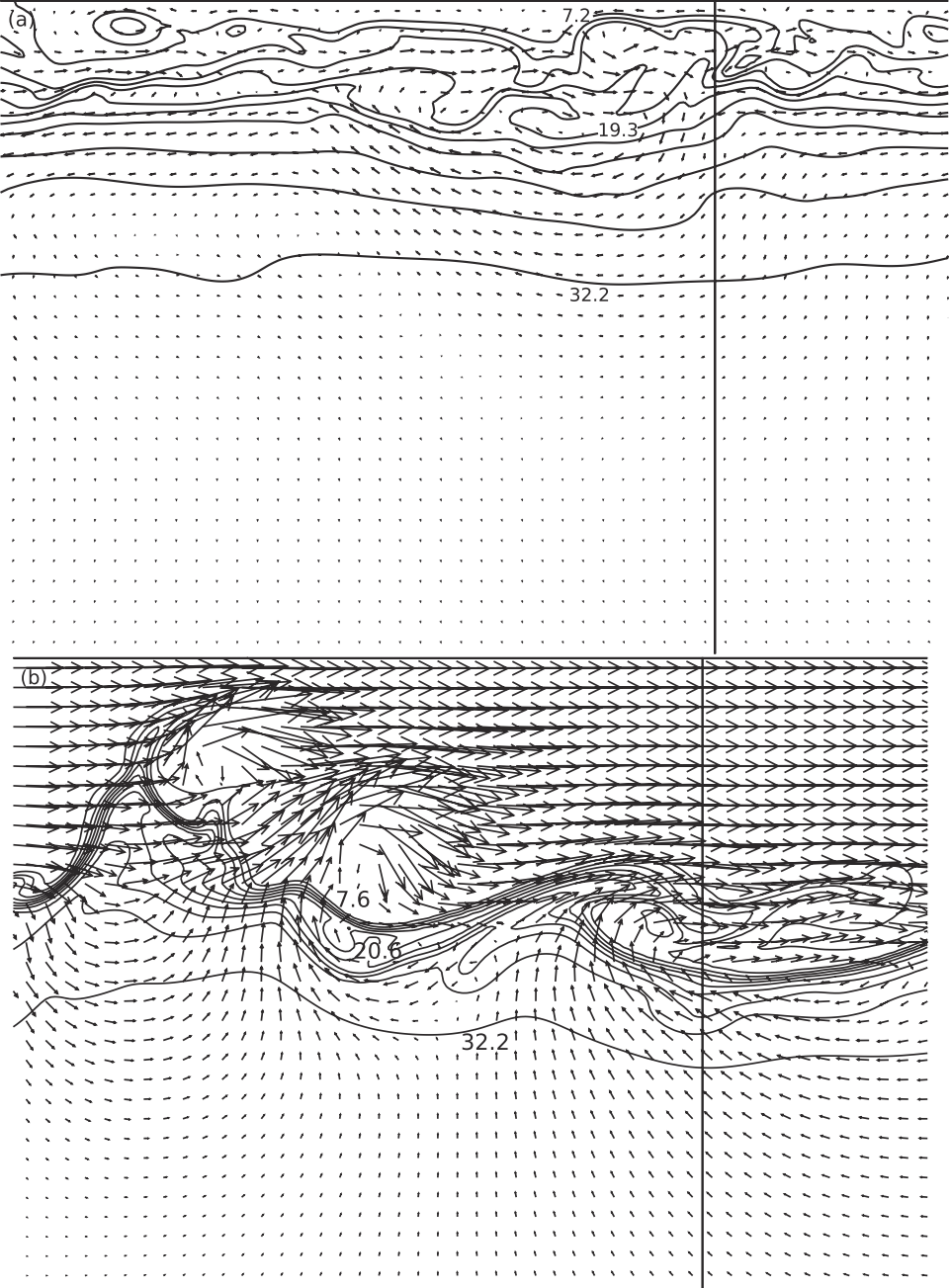
(a)
7.2
19.3
32.2
(b)
7.6
20.6
32.2

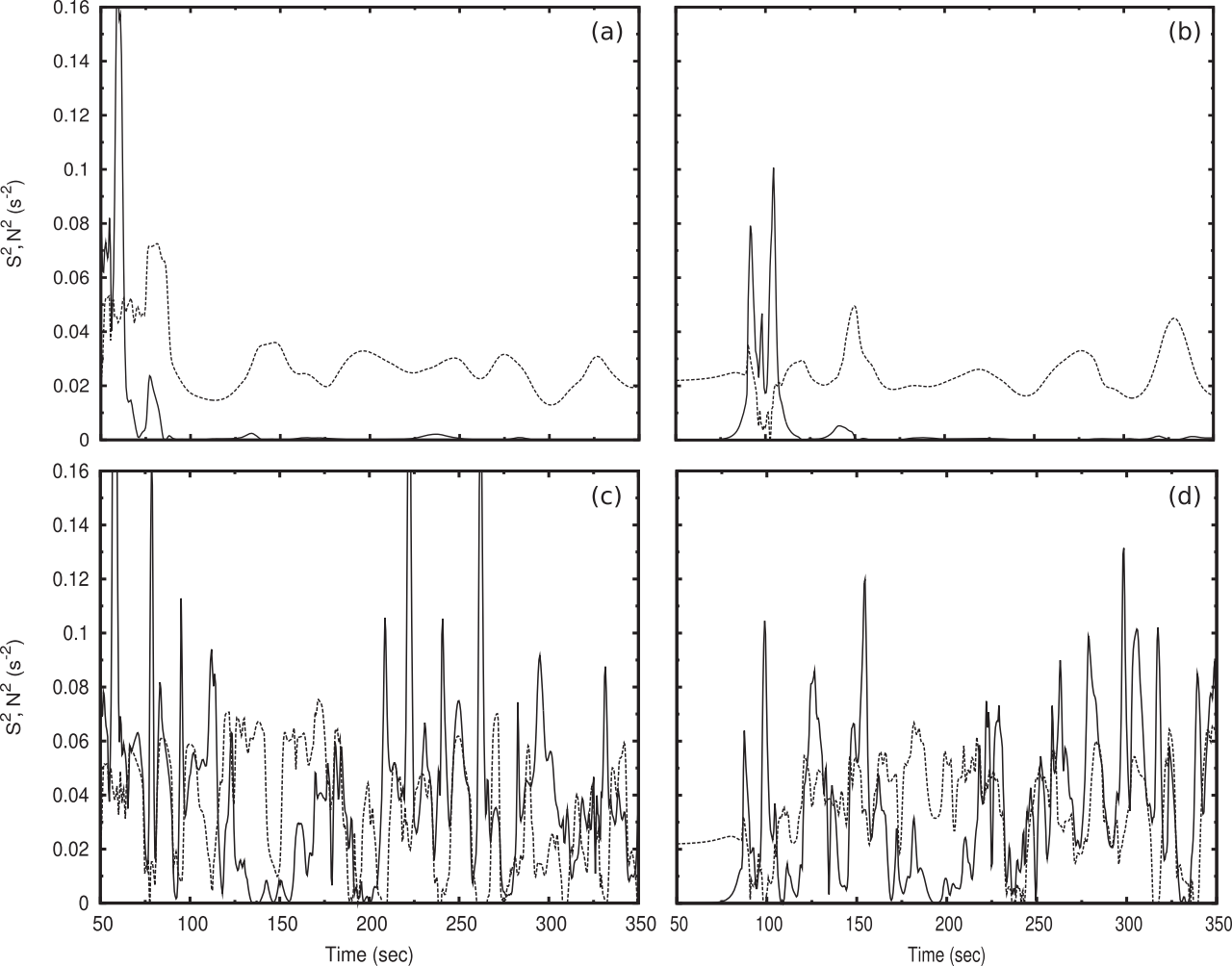
(a)
(b)
(c)
(d)
S^2, N^2 (s^{-2})
0
0.02
0.04
0.06
0.08
0.1
0.12
0.14
0.16
50
100
150
200
250
300
350
Time (sec)

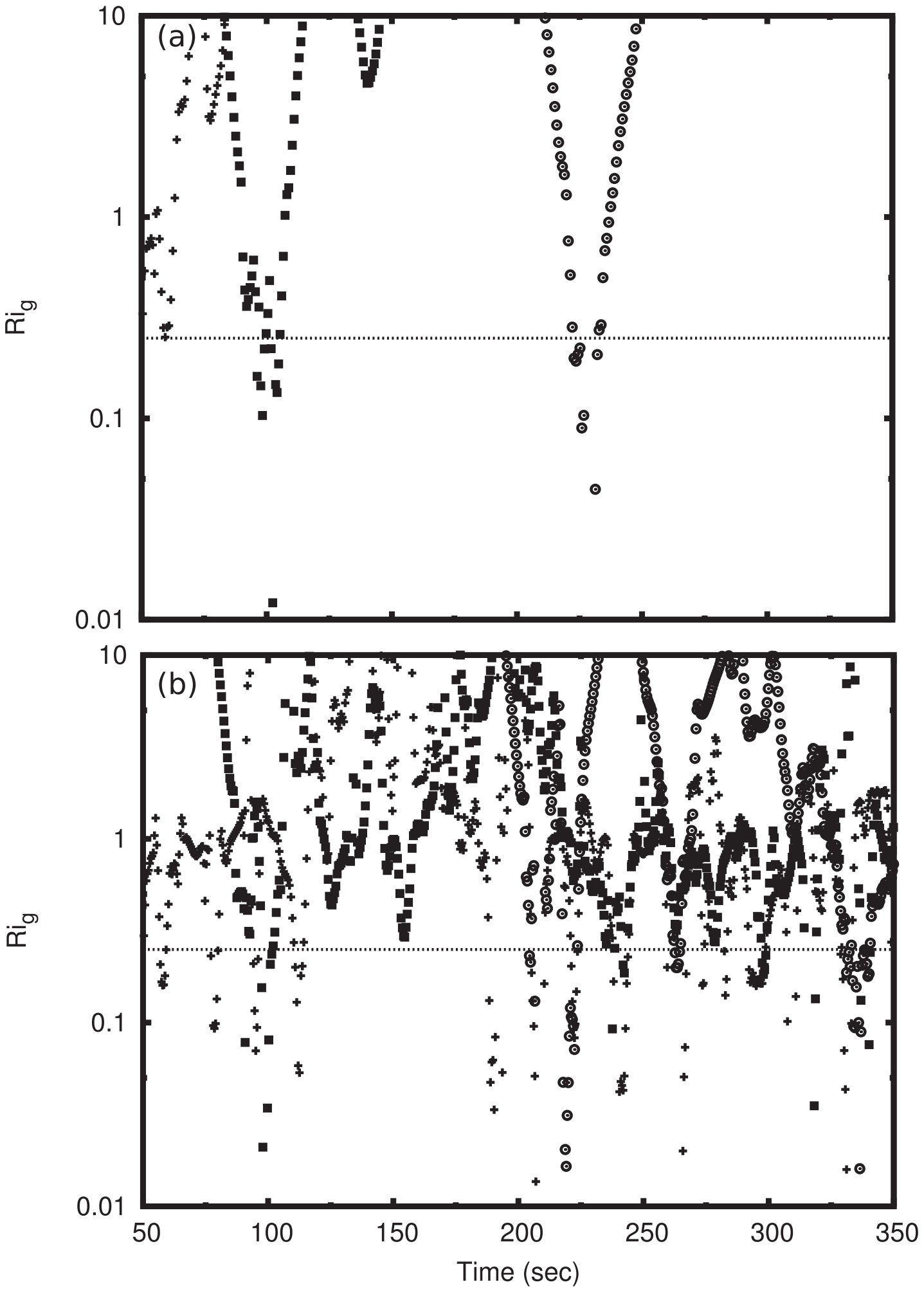
(a)
(b)
10
1
0.1
0.01
Ri_g
50
100
150
200
250
300
350
Time (sec)

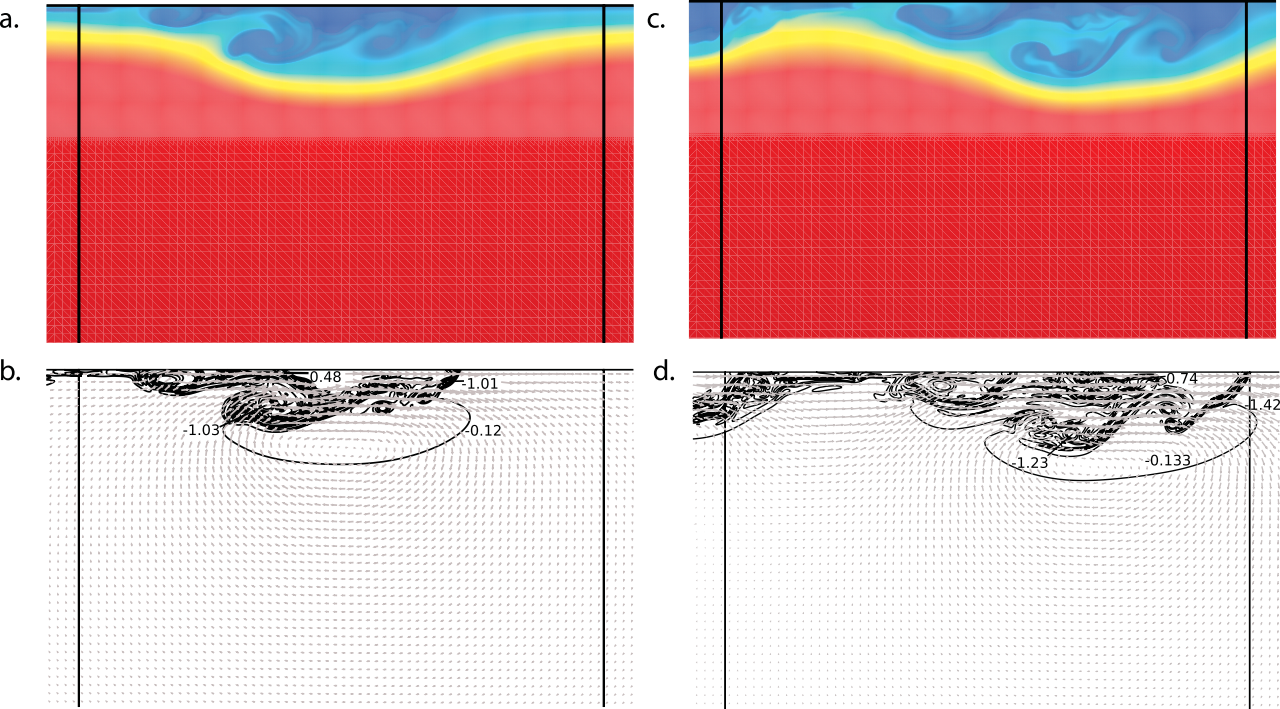
a.
c.
b.
d.
0.48
1.01
-1.03
-0.12
0.74
1.42
1.23
-0.133

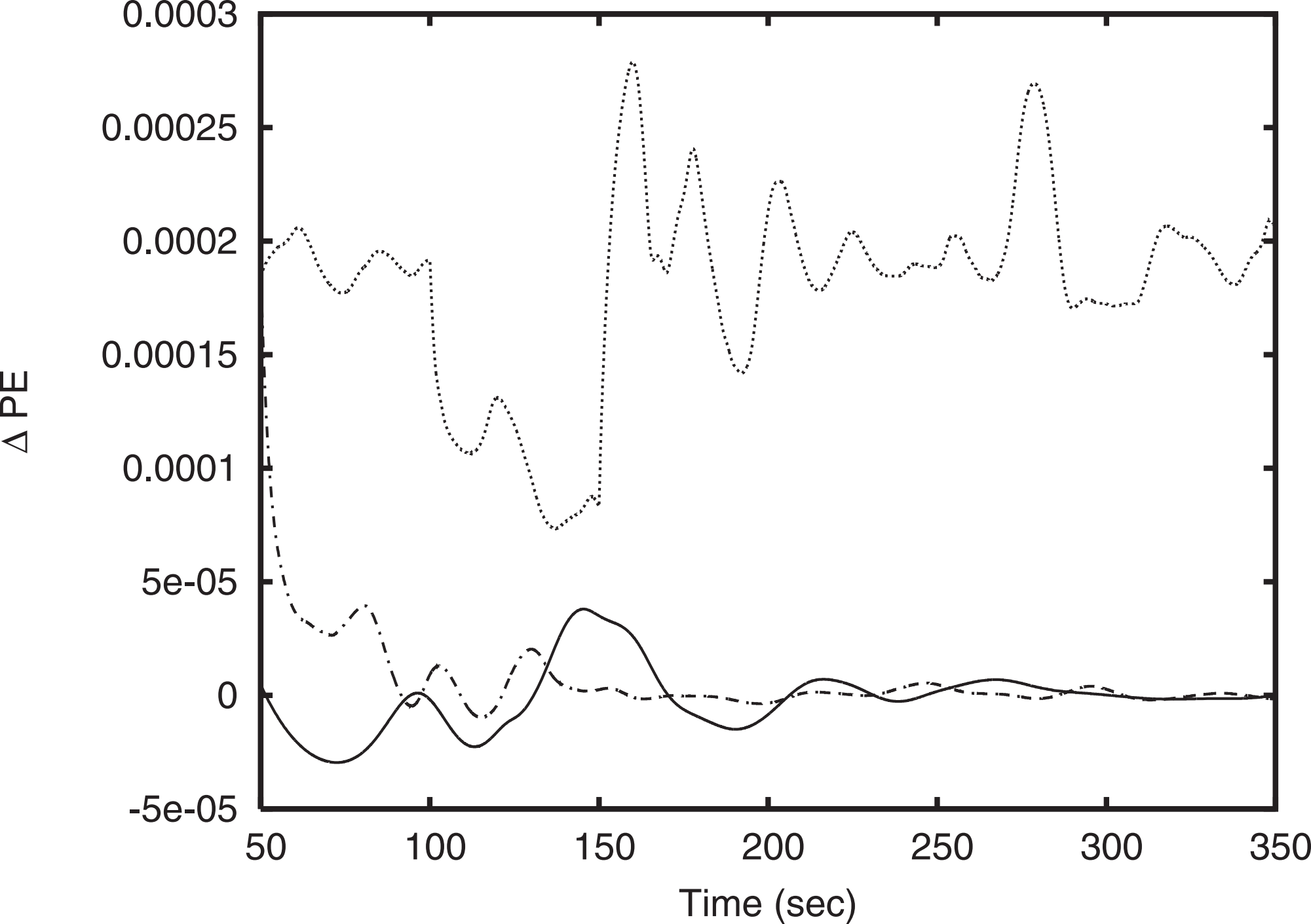
0.0003
0.00025
0.0002
0.00015
0.0001
5e-05
0
-5e-05
Δ PE
50
100
150
200
250
300
350
Time (sec)